Alma Mater Studiorum – Università di Bologna

School of Science

Department of Physics and Astronomy

Master Degree Programme in Astrophysics and Cosmology

Earthshine with High-Resolution Infrared Spectroscopy

Graduation Thesis

Presented by:

Yaren Hediye Bektaş

Supervisors:

Prof. Leonardo Testi
Università di Bologna

Dr. Michael Sterzik
European Southern Observatory (ESO)

Academic Year 2024/2025

Graduation Date 31 October 2025

"There are countless suns and countless earths all rotating around their suns in exactly the same way as the seven planets of our system.
We see only the suns because they are the largest bodies and luminous, but their planets remain invisible to us because they are smaller and non-luminous."

— Giordano Bruno, 1584

Contents

Acknowledgements

I would first like to express my deepest gratitude to Prof. Leonardo Testi for always being positive and motivating, not only during the thesis writing period but also throughout the semester. His inspiring lessons and guidance have been truly valuable to me. Dr. Michael Sterzik has been an exceptional mentor whose patience, clarity, and dedication deeply shaped this work. His ability to explain complex ideas with simplicity and precision, as well as his constant support and trust in my progress, have been the most important sources of growth and confidence during this project. I also thank Dr. Claudia Emde for providing the models essential for this study, and Dr. Giulia Roccetti for her insightful comments on my text, which greatly improved the final version. Finally, I would like to express my heartfelt appreciation to Dr. Taşkın Çay, who first planted in me the seeds of astrobiology during my undergraduate studies.

I am sincerely grateful to my family and friends for their endless love and support. To my mother Kibar, my father Gani, my sister Gülden, and my aunt Gülcan, thank you for believing in me unconditionally and always reminding me of where I come from. To all my friends, thank you for reminding me of life beyond academia; to laugh, to have fun, and to simply enjoy the moment.

Finally, I would like to express appreciation to myself, for the persistence to keep going, the curiosity that guided me, and the courage to grow through challenges. This thesis stands not only as a scientific achievement but also as a reflection of that personal journey.

Abstract

Biosignatures in the near-infrared spectrum of Earth's atmosphere include the simultaneous presence of O_2, CH_4, and H_2O molecular absorption bands. These molecules are important tracers of biological and atmospheric processes on Earth and provide useful analogs for exoplanet studies. High-resolution infrared spectra of Earthshine were obtained with the CRIRES+ instrument at the Very Large Telescope, which provides a resolving power of $R \approx 86{,}000$–$110{,}000$ for full-slit illumination. At this level, individual absorption lines can be resolved and studied in detail. Earthshine spectra contain the integrated light of Earth's illuminated surface and atmosphere reflected by the Moon. Therefore, they are considered similar to the unresolved spectra that would be observed from an exoplanet. In this work, Earthshine spectra were first divided by Sky spectra to minimize telluric effects and isolate the true disk-integrated Earth signal. The molecular absorption lines were then fitted with Gaussian profiles, and their properties were studied statistically through amplitude distributions and Kolmogorov–Smirnov and Anderson–Darling tests. The results show CH_4 and O_2 absorption features in the H band. Overall, this study shows that high-resolution Earthshine spectroscopy can be used to detect biosignature-related molecular features in disk-integrated spectra of Earth, and that statistical analysis of absorption-line properties provides valuable understanding of their detectability under exoplanet-like observing conditions.

Chapter 1

Introduction

The search for life beyond Earth is one of the most fascinating questions in science. Inspires curiosity within both the research community and among the public. In recent decades, one of the main goals of exoplanet studies has been to find Earth-like planets that locate within the so called habitable zone, where conditions could allow liquid water to exist. Determining whether such planets might be habitable requires knowledge of their atmospheres, particularly their chemical composition. The most direct way to access this information is through spectroscopy, as molecular absorption and emission features leave characteristic imprints in planetary spectra. In this way one can learn what gases are present, how strong their signals are, and whether they may indicate biological activity.

Our planet, Earth, is the only planet we know host life. Therefore, to understand the possibility of life beyond Earth, we must first learn from our own world; lessons that may one day reveal whether we are alone in the universe. Earthshine offers a rare observational perspective to study our planet as if it were observed from far away. This phenomenon occurs when sunlight reflects off Earth, illuminates the dark portion of the visible Moon, and is then reflected back to telescopes on Earth. The final spectrum contains light integrated over the entire planet, combination of contributions from both the surface and the atmosphere, and is therefore comparable to the unresolved spectra we obtain from exoplanets. In fact, Earthshine reproduces the same viewing geometry that we will use when observing exoplanets in reflected light [56].

Earthshine has been studied before, and features such as the vegetation red edge, ocean glint, and strong atmospheric absorption bands have been detected, e.g., [4, 46, 52]. An integrated spectrum of Earth has been obtained not only from the ground but also from space missions. Examples include Galileo [61] and EPOXI [36], which both provided disk-integrated spectra of Earth. In the infrared, EPOXI scanned its spectrometer slit across the entire Earth disc and then summed the signal to create a globally integrated spectrum. However, ground-based Earthshine observations have the advantage of being more accessible and sustainable, since the Moon can be used as a natural mirror of Earth without the need for a spacecraft. Another important advantage is that they offer a much broader phase coverage compared to spacecraft observations such as Galileo or EPOXI, which only observed Earth from a single or limited viewing geometry. As the Moon goes through its phases, different parts of the illuminated side of the Earth become visible, allowing us to observe Earth under many different lighting and viewing conditions. This makes it possible to study how the overall brightness and spectral features of Earth change with phase, helping us better interpret the reflected-light variations we might one day detect from exoplanets.

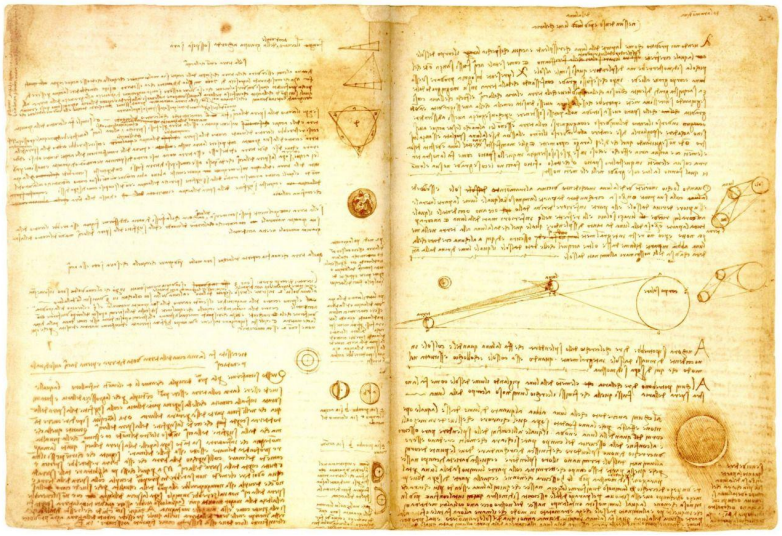

Figure 1.1: Leonardo da Vinci's sketch from the *Codex Leicester*, where he first explained the phenomenon of Earthshine in the early 1500s.

It is worth noting that the phenomenon of Earthshine was first correctly explained by Leonardo da Vinci in the early 1500s. In his notebooks (*Codex Leicester*), he described that the faint glow on the dark side of the crescent Moon is caused by sunlight reflected from Earth back onto the Moon [11]. Figure 1.1 shows one of his sketches that illustrates this concept.

More recently, advanced radiative transfer models and spectropolarimetric Earthshine observations have provided detailed simulations and measurements of Earth as an exoplanet [70, 71]. These models, developed by Emde and collaborators [17] and then extended by Roccetti et al. [56], introduce realistic cloud structures, surface reflectance, and polarization effects. All of these provide a framework to interpret Earthshine data. Together with spectropolarimetric observations, they show how features such as clouds, ocean glint, and the vegetation red edge shape disk-integrated spectra.

Building on these earlier studies, this thesis investigates molecular features that are directly relevant for biosignatures in the Earthshine spectra. While the initial focus of this work was on O_2, OH, and CH_4, the analysis was later broadened to include additional species such as H_2O, CO_2, and N_2O. Their detection across different infrared bands provides a more complete picture of Earth's atmosphere as an exoplanet analog.

The analysis follows a systematic approach. Absorption lines were identified and fitted with Gaussian profiles, and their parameter such as width, depth, and baseline offset were collected to study their statistical distributions. To account for telluric contamination, ratio spectra were constructed between Earthshine and Sky exposures, while Earthshine–Earthshine and Sky–Sky divisions were used as controls. Statistical tools, including cumulative distribution functions (CDFs), histograms, Kolmogorov–Smirnov tests, and Anderson–Darling tests, were then applied. In addition, the observed features were compared with model spectra developed by Emde et al. [17] to test their consistency.

The goal of this work is therefore not only to detect biosignature-related molecules in Earthshine, but also to measure their spectral properties, such as amplitude, width, and profile shape, using statistical tools and compare them with model predictions.

Chapter 2

Theory

Are we alone in the universe? This is not a question that only single field of science can answer. To address this question, the beauty of astrobiology emerges from the convergence of diverse scientific disciplines such as astronomy, biology, chemistry, and geology.

In this thesis project, I explore astrobiology from an astronomical perspective, focusing on the development of a method to detect biosignatures in Earth's integrated spectra. Biosignatures, simply put, are traces left behind by life. To understand what we are searching for, it is first essential to reflect on what life is. According to NASA's definition, "life is a self-sustaining chemical system capable of Darwinian evolution." [49] [12] This definition, combined with our current understanding of carbon-based life as the only known example, strongly influences how we search for life in the universe today.

Now that life has been defined, we now turn to the traces it may leave, biosignatures detectable in planetary spectra. Biosignatures have been widely discussed in the context of exoplanet research as indicators of biological activity (e.g., [68, 67, 13]). These biosignatures form the main focus of this study. However, interpreting biosignatures requires understanding the medium that shapes planetary spectra: the atmosphere. Earth's atmosphere absorption and scattering processes strongly influence Earthshine spectra. That is why a short overview of the atmosphere is useful before moving on to biosignatures.

2.1 Earth Atmosphere

2.1.1 Composition and Structure of the Modern Atmosphere

As shown in Table 2.1, Earth's atmosphere is made up largely of N_2, ∼78% and O_2, ∼21%, with smaller amounts of other gases. The gases that are interesting for biosignature studies are only present in small amounts, such as H_2O, CO_2, CH_4, N_2O, and O_3. These trace species, although present only in small amounts, leave characteristic spectral features that can be detected with different observational techniques. For example, Turnbull et al. [76] used the low-resolution CorMASS spectrograph (R $\sim$ 300) and were able to see broad bands of H_2O, O_2, and CO_2, as well as some weak CH_4 features in Earthshine spectra. In contrast, CRIRES+ provides a much higher resolution ($R \approx$ 86,000–110,000 for full-slit illumination) that allows individual absorption lines to be resolved [58]. This capability is essential for this thesis work, as it focuses on narrow spectral features such as O_2 and CH_4. It also shows how high-resolution spectroscopy can reveal fine details of atmospheric composition that remain hidden at lower resolution.

To interpret these spectral features correctly, it is also important to understand the physical and chemical behavior of the gases, such as their residence times in the atmosphere. The residence time of a gas describes how long, on average, a molecule stays in the atmosphere before it is removed by chemical reactions, biological processes, or physical mechanisms (see Table 2.1). Long-lived gases such as N_2 and O_2 have residence times of thousands to millions of years, which means they are well mixed throughout the atmosphere and their concentrations remain fairly stable. In contrast, short-lived species such as CO, H_2O, or OH have residence times ranging from days to seconds, so their abundances can change quickly with weather and local conditions. For this reason understanding residence times is important because it determines how a specific molecule contributes to the observed absorption features in Earth's spectrum.

Table 2.1: Major constituents and spectroscopically relevant trace gases of the modern Earth's atmosphere. Only gases that are dominant or important for biosignature studies are included here. Values adapted from Wallace and Hobbs (2006)[81].

Gas	**Content**	**Residence time**	**Major sources**
N_2	78.084%	1.6×10^7 yr	Biological
O_2	20.946%	3000–4000 yr	Biological
CO_2	0.042%	3–4 yr	Biological, oceanic, combustion
H_2O	0–4% (variable)	∼10 days	Evaporation, transpiration
CH_4	1.7 ppmv	9 yr	Biological, anthropogenic
N_2O	0.31 ppmv	150 yr	Biological, anthropogenic
O_3	10–100 ppbv	Days–weeks	Photochemical
CO	200 ppbv	∼60 days	Photochemical, combustion,anthropogenic
OH	0–0.4 pptv	∼1 s	Photochemical

In addition to its gaseous components, the atmosphere contains solid and liquid particles, including aerosols, cloud droplets, and ice crystals. These components are highly variable in space and time, and although they represent only a minor fraction of the total mass, they exert a major influence on radiative transfer, cloud formation, and the spectral characteristics of the atmosphere [35].

As can be seen in Fig. 2.1, the temperature, pressure, and density in Earth's atmosphere all change with altitude, and they define the main atmospheric layers where specific absorption lines originate. The troposphere, reaches up to about 10–15 km, contains most of the atmospheric mass and almost all of the H_2O. Above it, the stratosphere reaches up to about 50 km and hosts the O_3 layer. Here, O_3 is mainly produced by the Chapman mechanism: solar UV radiation splits O_2 into atomic oxygen, which then recombines with O_2 to form O_3. This process accounts for the majority of Earth's O_3 and produces a temperature inversion that causes the stratosphere to warm with altitude [24] [50].

Above the O_3 layer lies the mesosphere, where the temperature decreases again with altitude until reaching the mesopause, the coldest region of the atmosphere. In the upper part of the thermosphere, the temperature increases as a result of the absorption of solar radiation that causes the photodissociation of O_2 and N_2, as well as the photoionization of their atomic products. These processes contribute to the heating of the upper atmosphere and mark the transition toward the exosphere, where particles gradually escape into space [81].

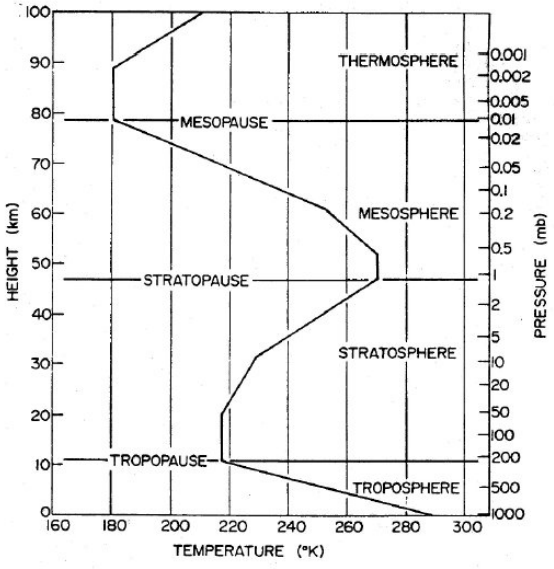

Figure 2.1: Typical vertical temperature structure of Earth's atmosphere.

As pressure decreases exponentially with altitude, the shape of absorption lines also changes: in the lower atmosphere, they are dominated by pressure broadening, and they show wider Lorentzian wings. On the other hand, at higher altitudes Doppler broadening becomes more important, and they produce a sharper core and weaker wings. Above about 40 km, both effects act together and are described by a Voigt profile [34].

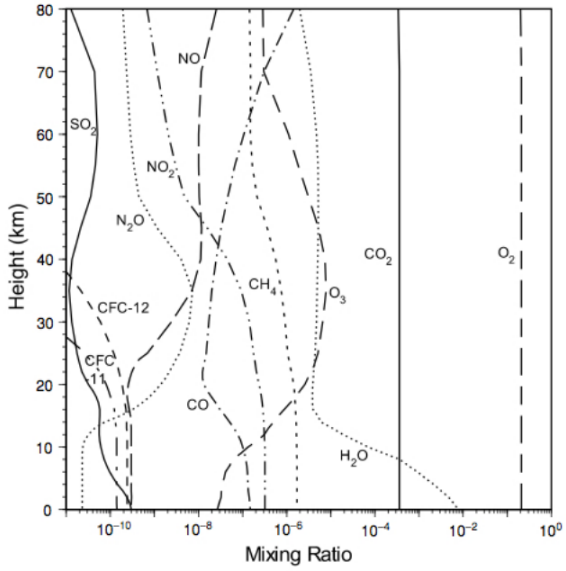

Figure 2.2: Vertical mixing-ratio profiles of selected atmospheric species in Earth's atmosphere, adapted from Vallis (2021) [78].

Not only do thermodynamic properties change, but also chemical abundances vary with altitude. The vertical distribution of these species is often described in terms of their *mixing ratio*, defined as the number of molecules of a given gas relative to the total number of air molecules at a given altitude [78]. As shown in Fig. 2.2, H_2O is highly concentrated in the lower troposphere, with over 90% confined below about 10 km. Its abundance, however, varies greatly in space and time; from around 10 ppm in the coldest regions of the atmosphere to as much as 5% by volume in hot, humid air masses [81]. O_3 is another variable component of Earth's atmosphere. Its concentration can fluctuate on daily to weekly timescales. Its abundance also varies with latitude and season, mainly due to changes in incoming solar UV radiation that control its photochemical production and destruction. In contrast to the highly variable species such as H_2O and O_3, gases like CO_2, CH_4, and N_2O are relatively well mixed throughout the atmosphere, with nearly constant concentrations up to about 80 km. [81].

2.1.2 Absorption and Emission

Radiation interacting with Earth's atmosphere is shaped primarily by absorption and emission processes, both are directly relevant to Earthshine observations.

Molecular absorption occurs at discrete wavelengths determined by quantized energy transitions. In the infrared, the strongest features arise from vibrational modes of molecules such as H_2O, CO_2, and CH_4, while O_2 contributes only weak IR features [22] [40]. These narrow absorption lines are central to biosignature detection, since their depth and profile provide direct information about atmospheric composition.

The atmosphere also produces emission, both thermal and non-thermal. A dominant non-thermal contribution is airglow which arises from photochemical reactions and excitations in the upper atmosphere. OH emission is particularly prominent at night, while O_2 emissions are UV driven, therefore, stronger during the day [79]. In the context of this thesis, absorption features in Earthshine spectra are the main focus, whereas emission lines have been analyzed in complementary work by Uhlmannsiek (2023) [77]. Understanding both processes, however, is important for interpreting how molecular signatures appear in the reflected and transmitted light from Earth's atmosphere.

2.1.3 Scattering, Reflection, and Transmission

In addition to absorption and emission, Earthshine spectra are shaped by scattering, reflection, and transmission processes. Scattering of electromagnetic radiation occurs whenever radiation interacts with matter that is inhomogeneous on the scale of the wavelength. This matter can be as small as a single electron, an atom, or a molecule, or as large as a solid or liquid particle. When illuminated by an electromagnetic wave, the electric charges inside the obstacle are set into oscillatory motion by the incident field. The accelerated charges then reradiate energy in all directions, producing what is observed as scattered light [6]. The dominant form of scattering in the visible is Rayleigh scattering, caused by molecules much smaller than the wavelength of light. Its λ^{-4} dependence makes shorter wavelengths scatter more efficiently, producing Earth's blue sky and the reddening of the Sun at sunrise and sunset [35].

At longer wavelengths, where particles are comparable in size to the wavelength, Mie scattering becomes important. This is primarily caused by aerosols such as dust, sea salt, or pollution, and results in broader, wavelength–independent scattering [6]. Mie scattering modifies the continuum level of Earthshine spectra, especially in the near-infrared, where absorption lines sit on top of a scattered background.

Emde et al. (2017) [17] studied Earthshine polarization spectra observed with the VLT/FORS2 instrument and compared them with MYSTIC radiative-transfer simulations. Their results showed that at wavelengths longer than about 750 nm, where aerosol (Mie) scattering becomes stronger, the continuum polarization becomes flatter and higher. In contrast, at shorter wavelengths, Rayleigh scattering dominates, and it produces a steeper continuum. This change in scattering behavior affects the overall continuum level of the Earthshine spectra.

Reflection from the Earth's surface also contributes significantly to the total Earthshine signal. Oceans, land, ice, and vegetation all have distinct reflectance spectra, which add to the combined Earthshine signal. For instance, oceans produce a generally dark background except for glint at certain angles [55], while vegetation imprints the sharp increase in reflectivity known as the Vegetation Red Edge (VRE) in the red part of the spectrum (Fig. 2.3) [4]. Snow and ice surfaces reflect light very efficiently across both

the visible and near-infrared wavelengths, giving them a very high albedo. In contrast, deserts and soils reflect more strongly in the near-infrared than in the visible part of the spectrum [35]. Clouds, through multiple scattering, raise the total planetary albedo and simultaneously dilute the narrow molecular absorption features that originate from transmission through the lower atmosphere [32]. Together, these surface and atmospheric processes shape the continuum level and the apparent depth of absorption lines seen in Earthshine spectra.

Finally, transmission through the atmosphere is what shapes the absorption bands themselves. Light that travels longer atmospheric paths (higher airmass or multiple reflections in Earthshine) experiences stronger attenuation [66]. This combination of scattering, reflection, and transmission creates the baseline on which individual absorption lines appear and explains why Earthshine spectra differ systematically from direct solar or Sky spectra.

2.2 Biosignatures

In astrobiology, a biosignature is broadly defined as an object, substance, or pattern whose origin specifically requires a biological process [14, 65]. In the context of exoplanet research, this typically refers not to the direct detection of life, which remains far beyond the capability of current technology, but rather to the identification of indirect evidence consistent with biological activity.

Related terms in the literature are sometimes used with different emphases. The word *biomarker*, common in geology and paleontology, refers to traces of past or present biological activity preserved in rocks, fossils, or other materials [72]. By contrast, *technosignatures* describe observable features specifically associated with advanced technology or intelligent life [73]. This work focuses solely on biosignatures detectable through planetary spectra, leaving out biomarkers and technosignatures.

Although there is no universally accepted classification, biosignatures are often grouped into three categories proposed by Meadows: gaseous, surface, and temporal [44]. Gaseous biosignatures arise from the activities of living organisms within a planet's atmosphere, surface biosignatures appear in the light reflected from life forms, and temporal biosignatures are changes over time linked to a planet's biological processes. In this thesis, the focus will be on gaseous biosignatures, since these are directly measurable with CRIRES+ infrared spectra, while surface and temporal biosignatures will be briefly introduced for completeness.

2.2.1 Gaseous Biosignatures

Atmospheric gases in a planet's atmosphere are often the first things one can target when searching for biosignatures. Unlike surface or temporal signatures, they can be detected at astronomical distances through spectroscopy at interstellar distances.

To understand what kinds of gases might work as biosignatures, it is useful to look at Earth's atmosphere and see how life has shaped its present composition. As discussed in Section 2.1, Earth's atmosphere is dominated by N_2 and O_2, with trace gases such as H_2O, CO_2, CH_4, and N_2O that are particularly relevant to biosignature studies [9]. These trace gases are interesting because many of them are linked to biological processes. What makes them even more meaningful is when they appear together in ways that are out

of chemical balance, for example O_2 and CH_4 existing at the same time. This kind of disequilibrium is hard to explain without life producing and maintaining it [37] [33].

It is important to remember that Earth's atmosphere did not always look like it does now. It has undergone major transformations over geological time. In the distant past, O_2 was almost absent while CH_4 was more common [29], which shows the focus should not be limited to thinking only of Earth's present-day atmosphere. Around 2.3 billion years ago, the Great Oxidation Event caused a major shift as O_2 started to accumulate due to photosynthetic life which led to intense changes in atmospheric chemistry and potential biosignatures [39] [7]. Even after this event, O_2 levels fluctuated for long periods before stabilizing near modern values [39]. These examples illustrate that planets can go through very different atmospheric stages, and life might still be possible under conditions unlike today's Earth. However, initiating the exploration of gases in the atmospheres of exoplanets with Earth-like compositions provides a reasonable starting point.

Another point to consider is the radiation from the host star, which can change how long biosignature gases survive in the atmosphere. Around M-dwarf stars, for example, lower UV radiation means gases like CH_4 and N_2O can stick around for long times and it is more probable to detect them [69, 59]. On the other hand, a planet with strong UV flux might destroy these gases more quickly, so their atmospheric abundance level reduces below observable levels [45]. Therefore, the absence of a certain gas in an atmosphere does not automatically mean the planet has no biosignature gases or life. It could simply mean that the biosphere is there, but its gases have short photochemical lifetimes and fall below detectability with our current observational capabilities.

Building on this, we can now delve into specific atmospheric biosignatures. While O_2 and CH_4 form the central focus of this work because of their strong potential as complementary biosignatures, other molecules detected in the dataset are also relevant. Species such as H_2O, CO_2, N_2O, and OH do not all qualify as direct biosignatures, but they provide essential context for understanding Earth's atmosphere as an exoplanet analog. For this reason, each of these gases is briefly introduced below.

Molecular Oxygen (O_2)

The presence of O_2 on Earth is almost entirely the result of photosynthesis. In particular, oxygenic photosynthesis (OP) uses light energy to split water molecules, producing O_2 as a by-product. The overall reaction is commonly written as:

$$\mathrm{CO_2\,(g) + 2\,H_2O + h\nu \rightarrow (CH_2O)_{org} + H_2O + O_2\,(g)} \tag{2.1}$$

where $(CH_2O)_{org}$ stands for organic matter, and $h\nu$ the energy of the incoming photons, with h is Planck's constant and ν their frequency.

One concern with O_2 is that it can be removed by reactions with reduced gases released from volcanoes. To keep a noticeable amount of O_2 in the atmosphere, the rate at which it is stored must be greater than the rate at which it is consumed. [8]

On Earth, small amounts of O_2 can be made without life by photolysis, where solar radiation splits oxygen-bearing molecules. However, this process is very slow and cannot build up a significant amount of O_2. This is because the distribution of UV energy from the Sun both controls how much O_2 is made and how fast it is destroyed, while geochemical sinks (such as reactions with reduced gases) remove what little O_2 is produced [25]. Therefore, the high levels of O_2 in Earth's atmosphere today are explained almost entirely by life. O_2 shows several strong absorption bands in the visible and near-infrared,

most notably the A-band at 0.76 µm and the 1.27 µm band, which includes both monomer and dimer (O_2–O_2) contributions [26, 54, 62]. The latter falls within the CRIRES+ J-band range used in this work.

Methane (CH_4)

As for CH_4, it is regarded as a potential biosignature mainly because it is produced by living organisms known as *methanogens* on our planet, as shown in the following reactions:

$$CO_2 + 4H_2 \longrightarrow CH_4 + 2H_2O \tag{2.2}$$

$$CH_3COOH \longrightarrow CH_4 + CO_2 \tag{2.3}$$

where CH_3COOH is acetic acid, a decay product from the fermentation of organic matter. On Earth, methane is mainly produced through these two pathways: either by respiring CO_2 with H_2 as in Equation 2.2, or by disproportionating acetic acid as in Equation 2.3. Methanogenesis is an ancient metabolism that only Archaea are able to perform, and it continues to be the main natural source of methane in Earth's atmosphere [74]. For this reason, methane is widely considered a potential biosignature gas, and its coexistence with O_2 is viewed as one of the strongest indicators of life, since these gases rapidly destroy one another and must be continuously replenished. This concept has been proposed as a potential biosignature [e.g., 38, 27, 61] and continues to be discussed in recent literature as one of the strongest indicators of biological activity [e.g., 33, 64].

However, CH_4 can also be produced abiotically, meaning that its detection alone is not sufficient to confirm life. Several abiotic mechanisms for methane generation have been proposed, including geological and planetary processes, which are reviewed in detail by Thompson et al. (2022) [75]. On Earth, however, such abiotic sources do exist, but they are orders of magnitude smaller than the biological flux from methanogens. This makes biology the overwhelmingly dominant source of atmospheric CH_4 [75]. What makes CH_4 especially compelling as a biosignature is not its presence by itself, but its long-term coexistence with oxidizing gases such as O_2 or CO_2, which is difficult to sustain without biological activity.

CH_4 shows absorption features across the visible to mid-infrared, with the strongest bands near 1.65 µm, 2.3–2.4 µm, and 3.3 µm, and additional weaker bands in the visible range. In the infrared, CH_4 absorption partially overlaps with H_2O and N_2O features, and it creates detection challenges at low spectral resolution [64]. However, the 1.65 and 3.3 µm bands are strong enough to be observed at high resolution, especially within the H and K bands of CRIRES+ used in this thesis work.

Nitrous Oxide (N_2O)

N_2O is primarily produced on Earth through biological activity, as an intermediate in the incomplete denitrification of nitrate (NO_3^-) to N_2 gas. A simplified scheme is:

$$NO_3^- \rightarrow NO_2^- \rightarrow NO + N_2O \rightarrow N_2 \tag{2.4}$$

With a relatively long atmospheric lifetime of ∼110 years, N_2O is nevertheless considered a promising biosignature because abiotic sources are extremely limited [61, 69, 53]. Its pre-industrial abundance was ∼270 ppb [48], with higher modern values due to anthropogenic activity. Photochemical models show that around M-dwarf stars, reduced UV

flux allows N_2O to accumulate more efficiently, potentially reaching higher concentrations than on present-day Earth [69, 53, 60]. In this sense, N_2O shows how both planetary and stellar context must be considered when evaluating possible biosignature gases [43, 28].

N_2O shows absorption bands near 3.7 µm, 4.5 µm, and 7.8 µm, with several weaker overtones between 1.3 and 4.2 µm [64]. Most of these features overlap with strong H_2O, CO_2, and CH_4 bands. Thus it is difficult to detect N_2O at low or moderate.

Other Contextual Species (H_2O, CO_2, OH)

Besides the primary biosignatures, several other molecules detected in the dataset are important for providing atmospheric context. H_2O, although not itself a biosignature, is critical for habitability and climate regulation [29]. Its absorption dominates large parts of the infrared spectrum and must be understood in order to correctly interpret weaker features. CO_2 is another major greenhouse gas that regulates planetary climate on long timescales and produces strong spectral bands that are relevant for comparative planetology [9, 23]. Finally, OH, while not a direct biosignature, is a key product of atmospheric photochemistry and it can still be useful as a tracer of the photochemical processes that control O_2 and O_3, which are both regarded as strong biosignature gases[83]. For these reasons, H_2O, CO_2, and OH are considered here as supporting species that help place biosignature detections into a broader atmospheric framework.

2.2.2 Surface and Temporal Biosignatures

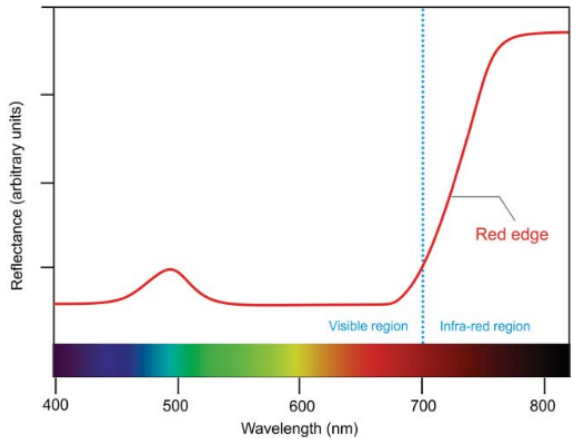

Figure 2.3: Schematic reflectance spectrum showing VRE. (Credits: Charles Cockell)

Living organisms can strongly affect a planet's surface spectrum. They do this through pigments that absorb and reflect light. One of the main impacts on a planet's surface is photosynthesis which transforms stellar energy into chemical energy. Chlorophylls, the green pigments present in photosynthetic organisms, capture light energy. The high-energy electrons, derived from chlorophylls, follow a sequence of electron carriers, and this leads to the conversion of water and carbon dioxide into glucose and O_2 (a redox reaction, as is typical in all life processes), see Eq. (2.1) [5]. As a direct result of photosynthesis, it is observable that one of the well-studied surface biosignatures on Earth: the Vegetation Red Edge (VRE), see Fig. 2.3. This distinct spectral characteristic arises due to the absorption patterns of chlorophyll, primarily in the red spectrum between 690 nm and 730 nm [68, 31]. This phenomenon is observable in the reflectance spectra of present-day Earth.

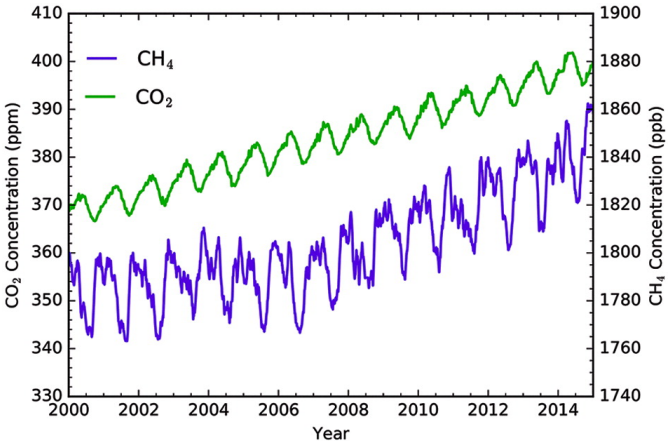

Figure 2.4: Gas abundance oscillations. These data were obtained from the NOAA's Earth System Research Laboratory.

Temporal biosignatures are observable fluctuations that indicate the influence of a biosphere on a planet's environment [63]. These variations can manifest as oscillations in gas concentrations or alterations in the planet's surface reflectivity. One well-known example is the seasonal variation in CO_2 concentration in Earth's northern hemisphere, linked to land biosphere productivity influenced by temperature and sunlight [30]. The CO_2 content of the atmosphere decreases in the spring as it is converted into organic matter through plant growth, while it begins to rise in fall and winter due to the decomposition of plant matter (see Figure 2.4). Modeling these changes involves complexities linked to planetary dynamics, such as axial tilt, orbital eccentricity, and surface heterogeneity. Thus, detecting gas fluctuations of a similar magnitude to those observed in Earth's present biosphere will be a considerable challenge and is likely beyond the capabilities of upcoming observatories.

While surface and temporal biosignatures represent important avenues for future research, their detection is beyond the scope of this work. In this thesis, they are introduced only for completeness.

Chapter 3

Methods

In this chapter, the observational strategy and data reduction procedures adopted in this thesis project are described. The description begins with the principle of Earthshine observations, followed by an overview of the CRIRES+ instrument, the observational runs at the VLT, and, finally the steps applied during data reduction.

3.1 Earthshine

Earthshine refers to the sunlight that is reflected by Earth onto the darker portion of the visible Moon and then reflected back to Earth, where it can be observed with a telescope. In this way, the Moon acts as a diffuse reflector (or simply a big mirror) that allows to be measured the disk-integrated spectrum of Earth.

Because the light has passed twice through the Earth's atmosphere, first on its way to the surface or clouds, and again after being reflected back toward the Moon, the resulting spectra contain strong atmospheric absorption features. The desired signal, analogous to the disk-integrated spectrum of an exoplanet, corresponds to the light emerging from the atmosphere after the first pass. The second pass introduces local telluric absorption that must be corrected.

As illustrated in Fig. 3.1, Earthshine observations represent a disk-averaged signal that includes both atmospheric transmission and surface reflection. Sunlight is first transmitted and scattered in the Earth's atmosphere, then reflected by Earth's surface and clouds toward the darker portion of the visible Moon of the Moon. The Moon reflects the light diffusely back toward Earth, where it can be detected by a telescope on the nightside of Earth. In practice, additional effects such as stray light contamination from the bright lunar crescent complicate Earthshine observations, but these are not shown in the figure for clarity.

Unlike direct observations of Earth's atmosphere from space, Earthshine measurements combine reflection from land, ocean glint, and cloud cover into a single unresolved spectrum, similar to how an exoplanet would appear in distant observations.

3.2 The instrument CRIRES+

CRIRES+ (CRyogenic high-resolution InfraRed Echelle Spectrograph) is the upgraded version of the original CRIRES instrument at the Very Large Telescope (VLT) in Paranal, Chile. It provides very high spectral resolution, up to $R \approx$ 86,000–110,000 for full-slit illumination, in the near-infrared range between about 0.95 and 5.3 μm, which covers

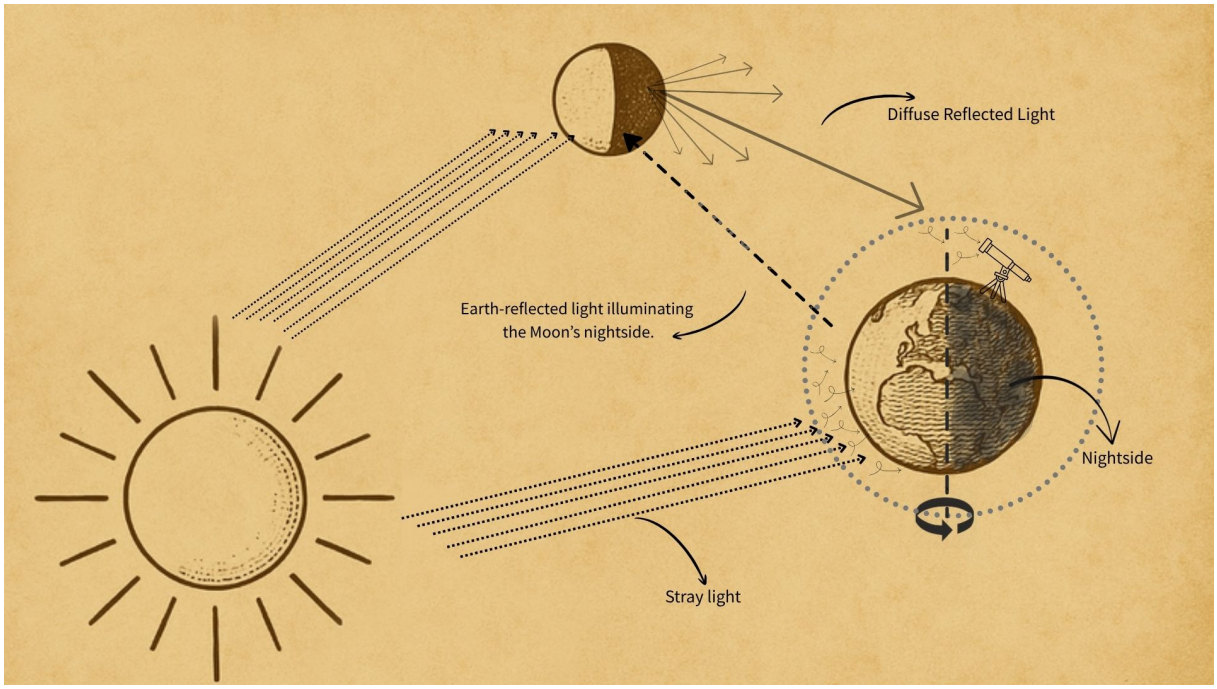

Figure 3.1: Schematic illustration of the Earthshine geometry.

the Y, J, H, K, L, and M bands. The adaptive optics system (MACAO) corrects the turbulent wavefront and provides diffraction-limited images at the focal plane; therefore, it improves the sensitivity for point sources by about a factor of two. Thanks to the new cross-dispersed design, CRIRES+ can record several spectral orders at the same time, which was not possible with the old single-order CRIRES [19], [58].

The instrument is equipped with improved detectors and a new calibration unit, including a laser frequency comb, and uranium-neon lamps. It also uses adaptive optics to improve the image quality. [18] These features make CRIRES+ ideal for studying narrow atmospheric absorption lines such as O_2, CH_4, and other interesting molecules. For this reason, it is an complete instrument for high-resolution Earthshine observations, where resolving individual lines is essential for identifying biosignatures and distinguishing them from telluric contamination.

3.3 Observations

The observations were performed during two runs, on 13–14 October and 12–13 November 2021, but in this work, only the November dataset was analyzed. The raw data are available in the ESO Science Archive [20], under program ID 0108.C-0927. The observing strategy differed between the two nights. In October, the telescope remained fixed on a single lunar position while the band-pass filters were exchanged sequentially. In November, by contrast, a more systematic sequence was followed: for each filter in turn (K2148, H1559, J1232, Y1028), the telescope cycled through all required positions. It began with a Moonshine (MS) reference on the illuminated side of the Moon, followed by Earthshine pointings close to the lunar center (ES A1) and near the limb (ES B1). Subsequently, three sky exposures were taken: Sky A1 close to the lunar disk, Sky B farther away, and Sky A2 again close to the disk. The sequence was then completed by returning to Earthshine at the limb (ES B2) and finally near the center (ES A2). The full pointing

scheme is illustrated in Figure 3.2.

A detailed extract of the November observation log, including time, position, exposure, and phase angle, is provided in Table 3.1.

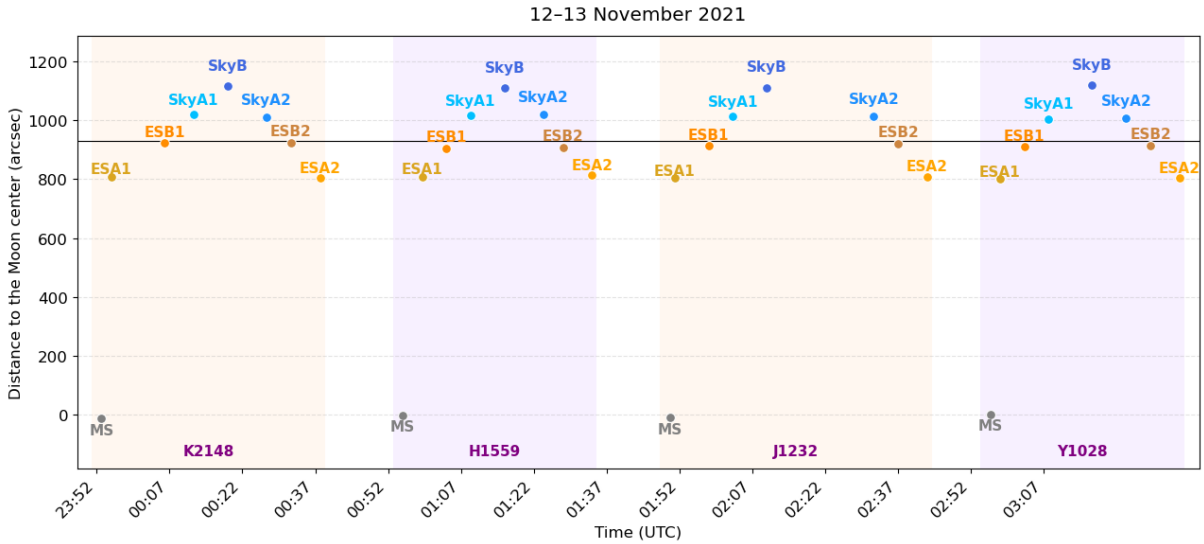

Figure 3.2: Time and pointing position of the telescope relative to the Lunar center. The black horizontal line represents the edge of the Moon.

As mentioned in Chapter 3.1, additional effects such as stray light contamination from the bright lunar crescent complicate Earthshine observations. For this reason, Moonshine observations are an important reference. Compared to Earthshine or Sky, they are dominated by the solar spectrum with only a weak contribution from airglow. Since part of the Moonshine is always scattered into the line of sight during Earthshine and Sky measurements, having a direct Moonshine spectrum is important for separating the solar and telluric components from the true Earthshine signal.

To illustrate the observing geometry during the J-band sequence, Earth and Moon views were generated by using the Earth & Moon Viewer (Fourmilab; [80]). In Fig. 3.3, panel (a) shows Earth as it appeared from the Moon at 00:37 UTC on 13 November 2021, corresponding to the start of J-band exposures. The display was set to *From Moon* with an altitude of 384,400 km, using the NASA Blue Marble map. Panel (b) shows the Moon as seen from Paranal Observatory (24°37'S, 70°24'W) at the same time, with the display set to *From Earth*, the location fixed to Paranal, and the Lunar Reconnaissance Orbiter texture was chosen. Together, the two images show the Earth–Moon configuration responsible for the Earthshine signal observed in the dataset analyzed in this study. Also, it can be seen from the Fig. 3.3, during the observations, Earthshine was dominated by reflection from the Pacific Ocean, which was on the day side of Earth.

3.4 Data Reduction

The raw CRIRES+ data were reduced using the official ESO CRIRES+ pipeline, following the procedure described in detail by Uhlmannsiek (2023) [77]. The reduction consisted of several standard calibration steps. First, dark frames were subtracted to remove detector bias and thermal signal, followed by flat-field correction to account for pixel-to-pixel sensitivity variations. A bad-pixel map was applied, and non-linear or defective pixels were

Table 3.1: Extract of the observation log for 12–13 November 2021.

Name	**Filter**	**Time (UTC)**	**Distance from Moon center (")**	**Exposure (s)**	**Phase angle (°)**
Moonshine	K2148	23:53	–	60.0	95.6
Earthshine A1	K2148	23:56	809	300.0	95.7
Earthshine B1	K2148	00:07	924	300.0	95.7
Sky A1	K2148	00:14	1022	300.0	95.7
Sky B	K2148	00:19	1117	300.0	95.8
Sky A2	K2148	00:25	1011	300.0	95.8
Earthshine B2	K2148	00:31	924	300.0	95.8
Earthshine A2	K2148	00:37	805	300.0	95.9
Moonshine	H1559	00:55	-2	60.0	96.0
Earthshine A1	H1559	00:59	809	300.0	96.0
Earthshine B1	H1559	01:05	906	300.0	96.0
Sky A1	H1559	01:11	1016	300.0	96.0
Sky B	H1559	01:16	1111	300.0	96.1
Sky A2	H1559	01:22	1021	300.0	96.1
Earthshine B2	H1559	01:27	999	300.0	96.1
Earthshine A2	H1559	01:33	814	300.0	96.2
Moonshine	J1232	01:50	-1	60.0	96.3
Earthshine A1	J1232	01:52	805	300.0	96.3
Earthshine B1	J1232	01:59	914	300.0	96.3
Sky A1	J1232	02:05	1015	300.0	96.4
Sky B	J1232	02:10	1112	300.0	96.4
Sky A2	J1232	02:30	1014	300.0	96.5
Earthshine B2	J1232	02:36	929	300.0	96.6
Earthshine A2	J1232	02:42	809	300.0	96.6
Moonshine	Y1028	02:56	1	60.0	96.7
Earthshine A1	Y1028	03:01	807	300.0	96.7
Earthshine B1	Y1028	03:04	915	300.0	96.8
Sky A1	Y1028	03:10	1006	300.0	96.8
Sky B	Y1028	03:17	1119	300.0	96.9
Sky A2	Y1028	03:22	1008	300.0	96.9
Earthshine B2	Y1028	03:28	913	300.0	96.9
Earthshine A2	Y1028	03:34	805	300.0	97.0

masked. Wavelength calibration was performed using exposures of uranium–neon (UNe) lamps and a Fabry–Pérot etalon. Finally, the pipeline extracted one-dimensional spectra from the raw two-dimensional echelle images.

Since the overall reduction strategy is identical to that of Uhlmannsiek (2023), the process is not repeated here in full; instead, the following sections describe only the analysis methods specific to this work. Figure 3.4 shows the reduced J-band spectra for all Earthshine and Sky observations, excluding Moonshine. The three detector chips are displayed to illustrate the overall data after pipeline calibration and extraction.

(a) Earth as seen from the Moon at 00:37 UTC, 13 Nov 2021 (J band window).

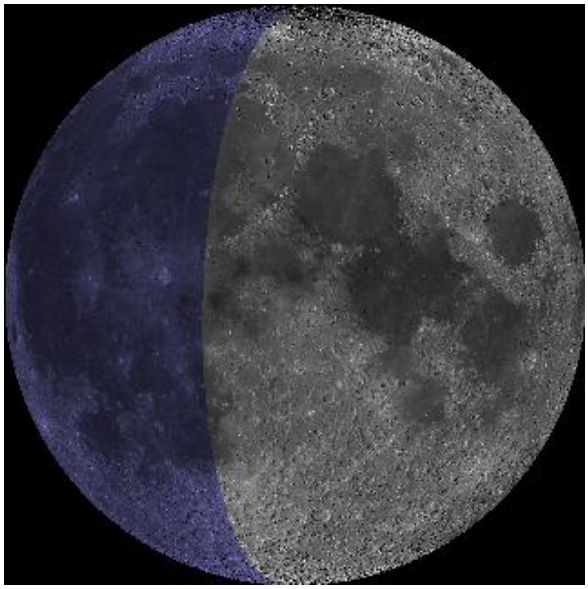

(b) Moon as seen from Paranal at the same time (waxing phase with Earthshine).

Figure 3.3: Earth–Moon geometry during the J-band observations on 13 Nov 2021. Images generated with the Earth & Moon Viewer (Fourmilab, John Walker).

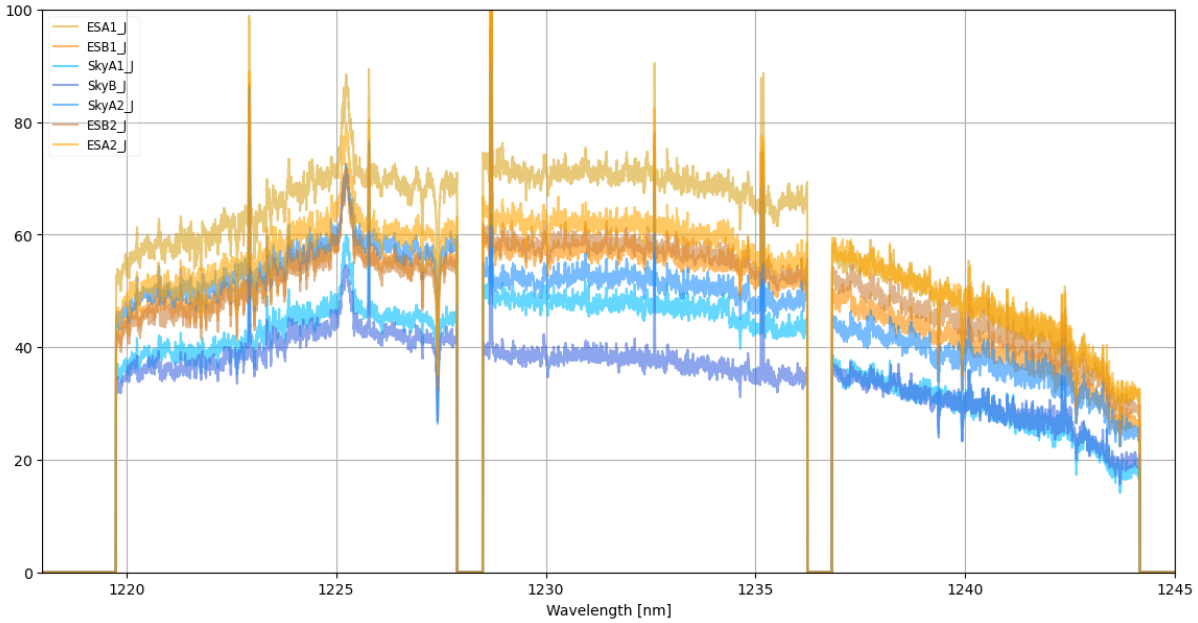

Figure 3.4: Reduced J-band spectra from all Earthshine and Sky observations (excluding Moonshine), shown for detector chips 1–3.

Chapter 4

Analysis

In this chapter, the analysis steps applied to the dataset are described, including the preparation and normalization of the spectra, removal of sky contributions, identification of molecular lines, and line fitting.

4.1 Preparation of Spectra

The starting point of the analysis was the one–dimensional spectra produced by the ESO Reflex reduction pipeline [21], described in the previous chapter. These spectra consist of flux as a function of wavelength for each of the three detector chips and all spectral orders recorded in a given exposure. For every observing position (Earthshine, Moonshine, and Sky), the reduced files therefore contained multiple spectral segments that covers the Y, J, H, and K infrared bands.

4.1.1 Line List from Atmospheric Transmission

Before performing Gaussian fits, a list of candidate absorption features was required. This was produced from an atmospheric transmission model which provides wavelength–dependent transmission values across the infrared. Local minima in the transmission curve were identified, corresponding to absorption dips due to molecular transitions. The central wavelengths of these minima were written into a plain text file (`linelist.dat`), which was then used as the input catalog for subsequent line fitting.

4.1.2 Line Fitting Routine

Prior to fitting, the flux values were scaled to counts per second by using the `EXPTIME` keyword in the FITS headers. Then, one-dimensional fits were performed around each candidate wavelength listed in `linelist.dat`. For a candidate line center λ^*, a fitting window:

$$\lambda^* - 0.1\,nm, \lambda^* + 0.1\,nm \tag{4.1}$$

was defined. Within this interval, a Gaussian absorption profile on a constant baseline was fitted:

$$F(\lambda) = 1 + \text{offset} - A \exp\left(-\frac{(\lambda - \mu)^2}{2\sigma^2}\right), \tag{4.2}$$

where A is the amplitude, μ is the line center, and the continuum level is represented by the offset. For a Gaussian absorption profile, the spread is characterized by the standard deviation σ. In spectroscopy, widths are commonly reported as the full width at half maximum (FWHM)[82, 51], with the conversion:

$$\sigma = \frac{\mathrm{FWHM}}{2\sqrt{2\ln 2}}. \tag{4.3}$$

All Gaussian parameters—amplitude A, line centre μ, FWHM, and baseline offset—were free parameters and therefore required initial guesses. The following choices were adopted:

(i) $A_0 = \max(F) - \min(F)$ within the fitting window (where F is flux);

(ii) μ_0 equal to the midpoint of the window, $\mu_0 = \frac{1}{2}(\lambda_1 + \lambda_2)$ with $[\lambda_1, \lambda_2] = [\lambda^* - 0.1\,\mathrm{nm},\ \lambda^* + 0.1\,\mathrm{nm}]$;

(iii) $\mathrm{FWHM}_0 = \lambda^*/R$ with $R = 100{,}000$;

(iv) the offset initialised to 0, then fitted freely.

In order to prevent the fitting routine from converging to unphysical values, parameter bounds were applied. The amplitude A was restricted relative to the initial guess A_0 obtained from the flux range in the fitting window, such that

$$A \in [0.1A_0,\ 4A_0].$$

The line center was constrained to remain within $\pm 0.05\,\mathrm{nm}$ of the seeded wavelength,

$$\mu \in [\lambda^* - 0.05,\ \lambda^* + 0.05],$$

while the FWHM was limited to the given interval

$$\mathrm{FWHM} \in [0.005,\ 0.5]\,\mathrm{nm}.$$

Finally, the continuum offset was allowed to vary within five times the estimated amplitude:

$$\mathrm{offset} \in [-5A_0,\ 5A_0].$$

Fitting was carried out using `scipy.optimize.curve_fit`, and returning best-fit parameters and their covariance. For each accepted fit, the following quantities were written into an output file: line center, amplitude, FWHM, offset, least squares, and parameter errors.

A minimum of ten spectral pixels was required within the fitting window. Candidate lines with fewer points were skipped, since such sparse sampling would not provide a stable or reliable fit. Lines with FWHM $\notin [0.02, 0.5]\,\mathrm{nm}$ were rejected, as were fits with a reduced squares greater than 2.0. The routine automatically produced one output file per exposure (e.g. `fit_results_ESA2_H.txt`).

The fit statistic implemented in the code was defined as:

$$\mathrm{LSQ2}_\nu = \frac{1}{\nu}\sum \frac{(F_{\mathrm{data}} - F_{\mathrm{model}})^2}{F_{\mathrm{model}}}, \tag{4.4}$$

where ν is the number of degrees of freedom. This is not equivalent to the standard reduced chi-squared,

$$\chi^2_\nu = \frac{1}{\nu} \sum \frac{(F_{\text{data}} - F_{\text{model}})^2}{\sigma^2}, \tag{4.5}$$

where σ denotes the noise level in line-free regions. The current form should therefore be regarded as a least-squares statistic. The reduced chi-squared statistic requires known uncertainties σ_k for each data point, which were not available for the spectra used in this analysis. As the noise level could not be reliably estimated for individual pixels, the χ^2_ν statistic would not provide meaningful weighting of the residuals. Therefore, a least-squares (LSQ) approach was applied, minimizing the squared differences normalized by F_{model}, to ensure stable fits in the absence of precise error estimates.

Examples of individual fits are shown in Fig. 4.1, while the total numbers of accepted fits in each band and observation are listed in Table 4.1. In total, a few thousand lines passed the acceptance criteria across all bands. These fitted parameters provide the starting point for the following analysis.

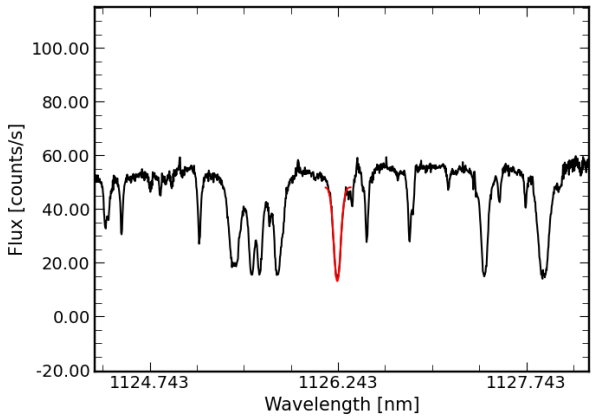

(a) Example fit 1. The black curve is the observed spectrum; the red curve is the best-fit Gaussian within the fitting window.

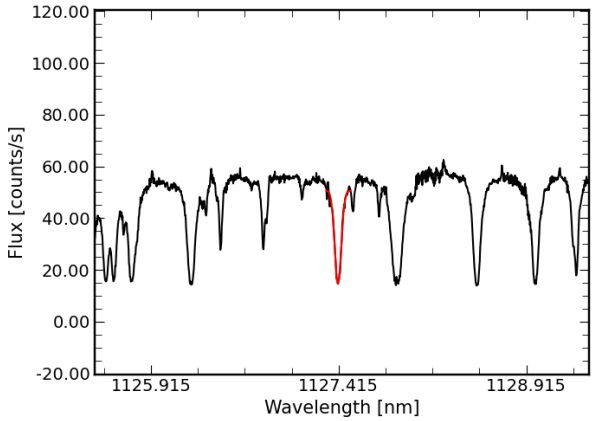

(b) Example fit 2. Same conventions as panel a.

Figure 4.1: Gaussian line-fit examples. Black: observed spectrum. Red: best-fit Gaussian over the defined window.

Table 4.1: Number of accepted Gaussian fits per exposure in each band.

K band	
ESA1	111
ESA2	127
ESB1	126
ESB2	146
MS	16
SkyA1	121
SkyA2	132
SkyB	156
TOTAL	**935**

H band	
ESA1	129
ESA2	169
ESB1	172
ESB2	198
MS	21
SkyA1	195
SkyA2	242
SkyB	212
TOTAL	**1338**

Y band	
ESA1	94
ESA2	117
ESB1	129
ESB2	129
MS	11
SkyA1	117
SkyA2	147
SkyB	148
TOTAL	**892**

J band	
ESA1	188
ESA2	209
ESB1	230
ESB2	219
MS	11
SkyA1	251
SkyA2	218
SkyB	267
TOTAL	**1593**

4.2 Statistical Analysis of Fit Parameters

After collecting all accepted Gaussian fits, the next step was to analyze the distributions of the fitted parameters. For this purpose, histograms and cumulative distribution functions (CDFs) were generated for four quantities: FWHM, amplitude, wavelength shift ($\Delta\lambda$), and continuum offset. The histogram represents the frequency distribution of the quantities. The CDF complements this by showing the cumulative fraction of lines below a given value, which makes it easier to understand the analysis.

4.2.1 FWHM

The FWHM represents the measured width of each fitted spectral line. In practice, the minimum width that can be observed is limited by the instrumental resolution, so the resolving power of the spectrograph sets the natural reference scale for this quantity. The resolving power of a spectrograph is defined as:

$$R = \frac{\lambda}{\Delta\lambda}, \tag{4.6}$$

where $\Delta\lambda$ is the minimum wavelength separation between two resolved features. The quantity $\Delta\lambda$ therefore sets the scale of the instrumental FWHM, such that

$$\mathrm{FWHM}_{\mathrm{inst}} \approx \frac{\lambda}{R}. \tag{4.7}$$

At $R \simeq 100{,}000$ for CRIRES+, the instrumental contribution to the line width is of order $\Delta\lambda \sim 10^{-2}\,\mathrm{nm}$. For example, in the J band at $\lambda \approx 1250\,\mathrm{nm}$, the expected instrumental width is

$$\Delta\lambda = \frac{\lambda}{R} \approx \frac{1250}{100{,}000} = 0.0125\,\mathrm{nm}.$$

This value represents the narrowest FWHM that can be measured, even for intrinsically unresolved atmospheric lines, since the instrument itself broadens them to this scale.

In the fitting routine, this relation between FWHM and resolution was used to provide a reasonable initial guess. For each candidate line, the initial width was set as shown in Eq.(4.7).

The fitted FWHM distributions for all four bands are shown in Fig. 4.2. In all cases, the values are broader than the instrumental lower limit, which means that the widths are not only set by the resolution of the spectrograph, but also by additional effects.

In the Earth's atmosphere, line broadening can happen for different reasons. Doppler broadening is caused by the thermal motions of molecules, while pressure (collisional) broadening becomes important at higher pressures [35]. Since the observed telluric absorption features are formed at different altitudes in the atmosphere, both Doppler and pressure broadening can contribute to the measured line widths. In the upper atmosphere, where the pressure is very low, Doppler broadening is expected to dominate, while for lines that originate lower in the atmosphere, pressure broadening may become more relevant. In practice, the fitted FWHM values therefore reflect a combination of instrumental resolution and these broadening mechanisms.

Figure 4.2 shows, for each band, the histogram of fitted FWHM (bars, left axis) together with the cumulative distribution function (CDF; coloured lines, right axis). The fitted line widths increase with wavelength: the Y-band distribution sits at the smallest values, J shifts slightly to the right, and H and K are clearly broader, i.e., the CDFs move rightward from Y to K. Within each band, the Earthshine and Sky samples overlap closely, which indicates no systematic difference between observing positions. To sum up, the plots indicate that the fitted widths are physically reasonable, increase as expected with wavelength, and are consistent between the Earthshine and Sky datasets.

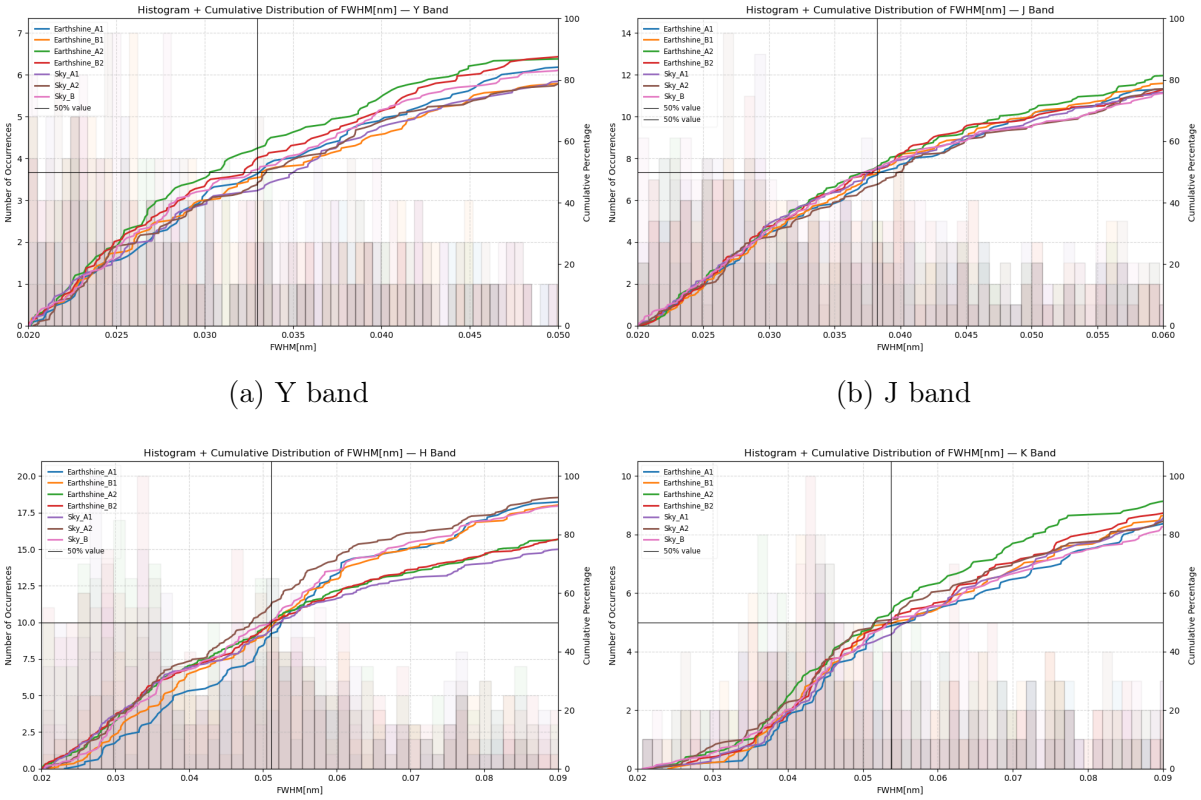

(a) Y band

(b) J band

(c) H band

(d) K band

Figure 4.2: Histograms and CDFs of fitted FWHM for Y, J, H, K bands.

4.2.2 Wavelength Shift ($\Delta\lambda$)

The wavelength shift ($\Delta\lambda$) measures the difference between the fitted line centers and the reference wavelengths from the linelist. This diagnostic was used to test for possible systematic effects in the fitting procedure. A distribution centered around zero indicates that the fitted lines are well aligned with the reference, while systematic deviations would point to potential biases.

The histograms and cumulative distributions of $\Delta\lambda$ for the Y, J, H, and K bands are shown in Figure 4.3. In all cases, the distributions are narrow and centered close to zero, and this suggests that the wavelength calibration and shifting routine worked reliably. The scatter of the fitted line centers is typically within ± 0.01 nm.

A small Doppler shift could, in principle, be expected in the Earthshine spectra because the absorption lines are produced on the dayside atmosphere (over the Pacific), which has a non-zero rotational velocity toward the Moon. In contrast, the Sky spectra are formed only in the local atmosphere above Paranal, which co-rotates with the telescope, so no rotational shift is expected there. Therefore, in the CDF of wavelength shift one would expect a larger shift for ES and almost no shift for SKY; again, in principle, this should be detectable with CRIRES+, which has sufficient capability. It can be seen from the following equations that the expected ES shift scales as

$$v_{\text{eq}} = \frac{2\pi R_{\oplus}}{T},$$

where $R_{\oplus} = 6378$ km is the Earth's radius and $T = 24 \times 3600$ s is the rotational period. This corresponds to

$$v_{\text{eq}} \approx 464 \text{ m s}^{-1}.$$

The associated wavelength shift can be estimated from the Doppler formula

$$\Delta\lambda = \frac{v}{c} \cdot \lambda,$$

which at $\lambda = 1000$ nm gives

$$\Delta\lambda \approx \frac{464}{3 \times 10^8} \times 1000 \text{ nm} \approx 1.5 \times 10^{-3} \text{ nm}.$$

As a result, at $\lambda = 1000$ nm a 1.5×10^{-3} nm shift is expected from Earthshine; with CRIRES+ ($R \approx 10^5$) such a shift is, in principle, detectable. However, in this dataset, no shift is detected. In other words, there is no visible difference between CDF of the ES observations and Sky observations in Fig.4.3.

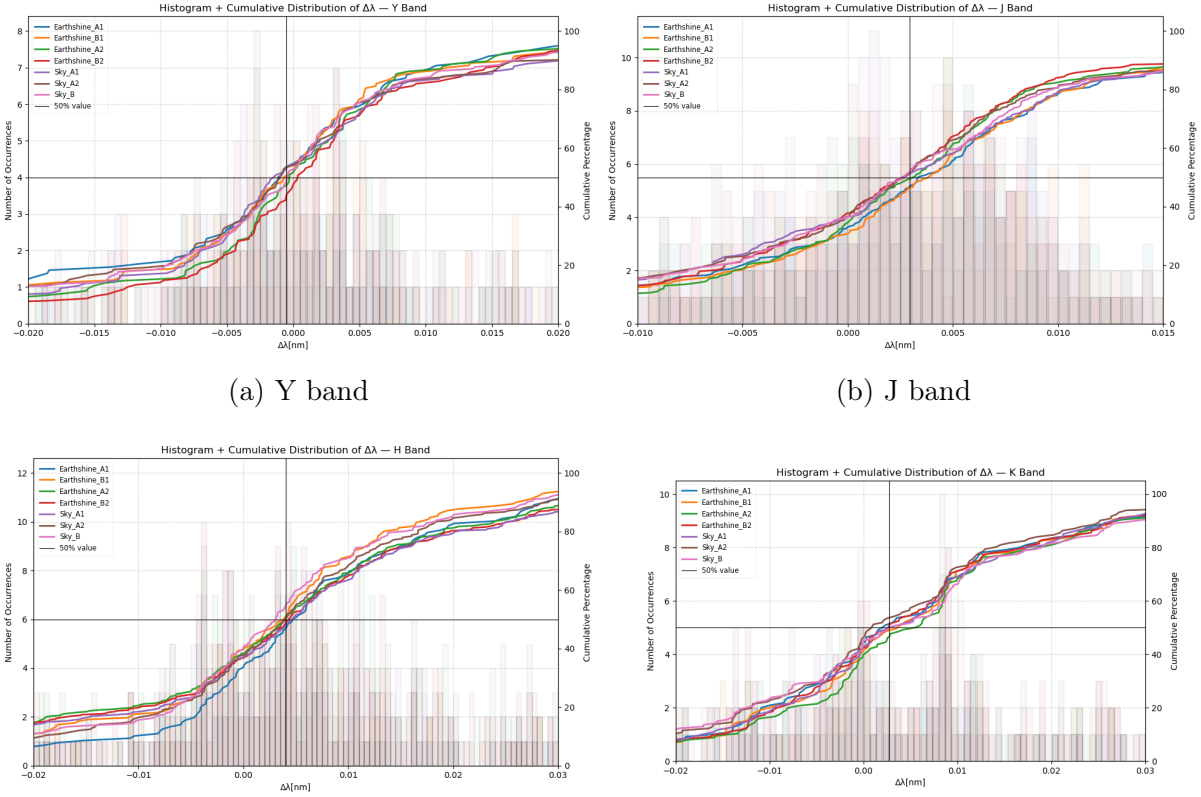

(a) Y band

(b) J band

(c) H band

(d) K band

Figure 4.3: Histograms and CDFs of $\Delta\lambda$ for Y, J, H, K bands.

4.2.3 Amplitude

The amplitude represents the depth of an absorption line relative to the continuum. It is therefore a direct measure of line strength. Examining the amplitude distribution provides a way to test whether certain observation positions, such as ESA1, ESA2, or Sky, produce systematically stronger or weaker absorption. In addition, comparing the results band by band allows one to determine whether these trends remain consistent throughout the all spectral range or whether variations appear in specific regions.

Figure 4.4 shows the distribution of fitted amplitudes in the Y, J, H and K bands. It can be seen that the Earthshine exposures (ESA1, ESA2, ESB1, ESB2) extend toward systematically higher amplitudes compared to the Sky spectra (SkyA1, SkyA2, SkyB). This behaviour is expected, since Earthshine light passes through the Earth's atmosphere twice. As a result, the absorption lines in Earthshine spectra appear deeper than in the direct Sky observations.

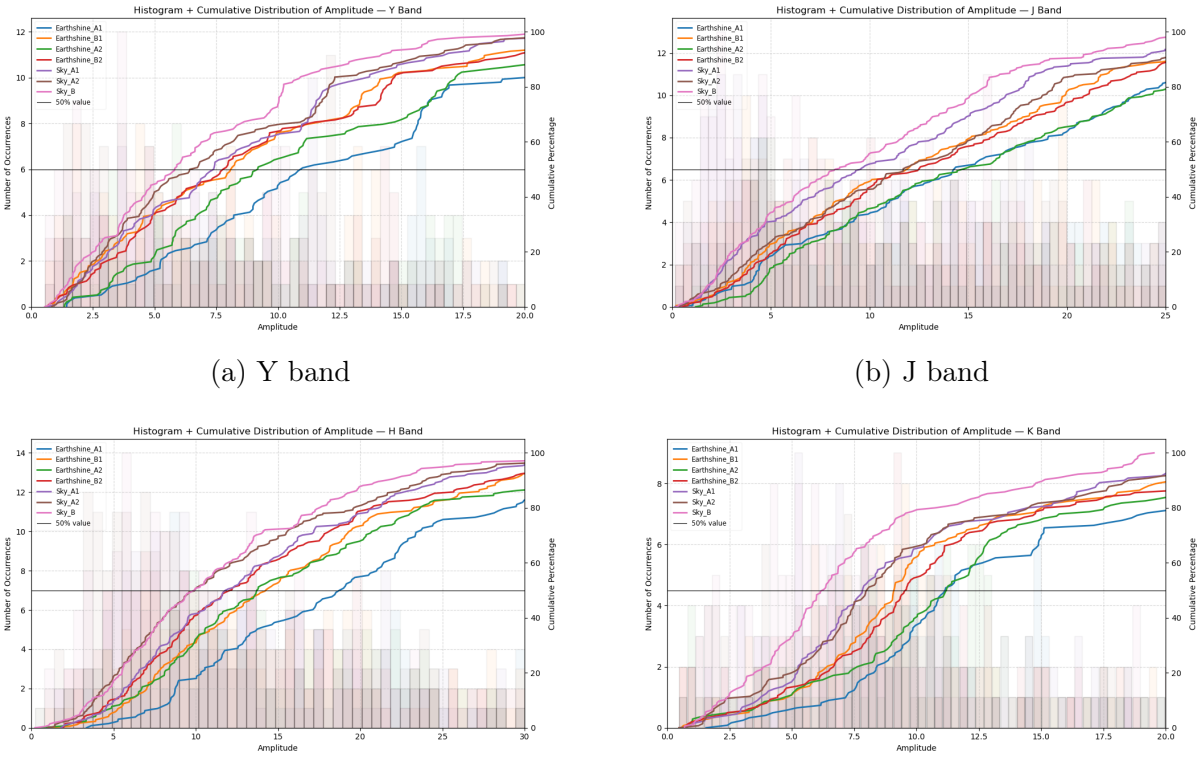

(a) Y band

(b) J band

(c) H band

(d) K band

Figure 4.4: Histograms and CDFs of fitted amplitudes for Y, J, H, K

4.2.4 Continuum Offset

The continuum offset parameter that indicates the local flux baseline against which absorption lines are fitted. The continuum offset is directly linked to the amount of scattered light present in the observations. Scattered light contributes an additional background that increases the overall flux level without carrying absorption features, which leads to higher continuum offsets. This effect is expected to be stronger in the Earthshine spectra, where scattered contributions from the Moon and the Earth's atmosphere are more significant than in the direct Sky exposures. Figure 4.5 shows the histogram and CDF of the fitted offsets for all bands that illustrates how the baseline levels differ between observing positions, and between bands.

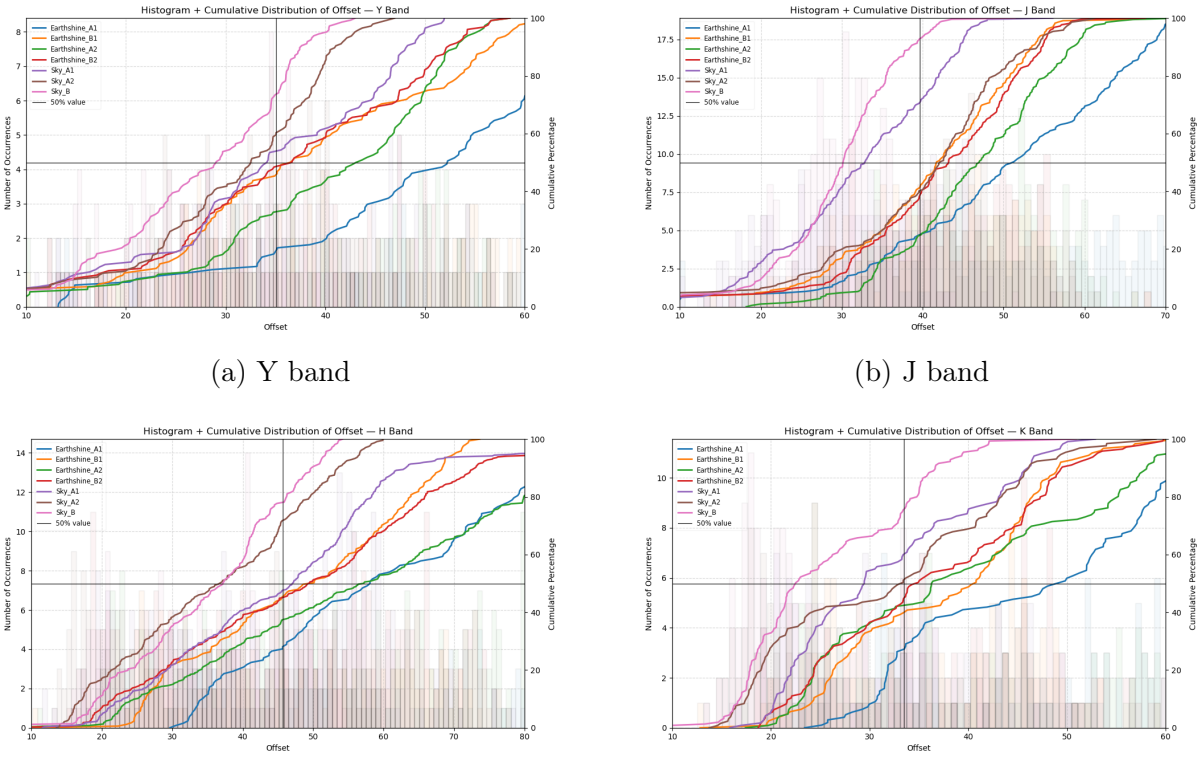

(a) Y band

(b) J band

(c) H band

(d) K band

Figure 4.5: Histograms and CDFs of fitted offsets for Y, J, H, K bands.

4.3 Ratio Spectra

Direct Earthshine spectra are strongly affected by telluric absorption, as the light passes twice through the Earth's atmosphere before reaching the telescope. In Earthshine observations, only the second atmospheric pass, when the light re-enters the atmosphere on its way to the observer, contributes to the telluric absorption that must be corrected. The first pass, during which sunlight is transmitted through and reflected by Earth's surface and clouds, is considered part of the planetary signal to be measured. To correct for the second-pass absorption, ratio spectra were constructed by dividing the Earthshine spectra by the Sky exposures. Since both observations share nearly identical atmospheric transmission during the second pass, most of the telluric absorption is cancelled in the ratio. The remaining signal primarily represents the true Earthshine component, allowing the real planetary spectrum to be isolated from the effects of the local atmosphere.

For each detector chip and spectral order, the valid wavelength range was taken directly from the FITS headers. As described in Section 4.1.2, the flux values were first scaled to counts per second by dividing by the header keyword `EXPTIME`. Then, within the valid range of each order, the flux of every exposure was normalized by dividing by the median value, so that the local continuum is approximately unity on an order-by-order basis.

Rather than combining all available Earthshine frames into a single spectrum, only selected exposures were used. Each selected Earthshine spectra were paired with the most reliable Sky spectra, and ratio spectra were obtained by dividing Earthshine by Sky. Why these combinations were chosen will be described in the following section.

4.3.1 Selection of Exposure Pairs

The first attempt to find the best pairs used the continuum offset diagrams (see Fig. 4.5). Focusing on the J band, the first candidate pairs were the extremes: the brightest Earthshine couple (ESA1/ESA2) and the darkest Sky couple (SkyA1/SkyB). The expectation for the ratio spectra was the following: since ES/ES and Sky/Sky should cancel their common signals, these diagnostic ratios would be featureless, while the main signal should appear in the ES/Sky spectrum. However, as seen in Fig. 4.6a, while Sky/Sky spectra cancelled the ES/ES division spectra did not fully cancel; some residual features remained. As a result, additional selection and stability checks were required.

To visualize the observation positions, Fig. 4.6b shows the pointings: the y–axis is the angular distance from the Moon's centre (arcsec), the horizontal line marks the lunar radius, times are UTC, and red circles highlight the frames used in the ratio spectra.

After the offset–CDF pairing gave unreasonable results, a trial-and-error procedure was adopted. Several Earthshine pairs were tested while the Sky positions were kept fixed, as it was already canceled. The final pair selected was (ESA2 and ESB2). In Fig. 4.7a, the ES/ES diagnostic ratio is essentially flat, and it indicates that the background has been cancelled. Therefore, the blue ES/Sky spectrum is interpreted as the true Earthshine signal.

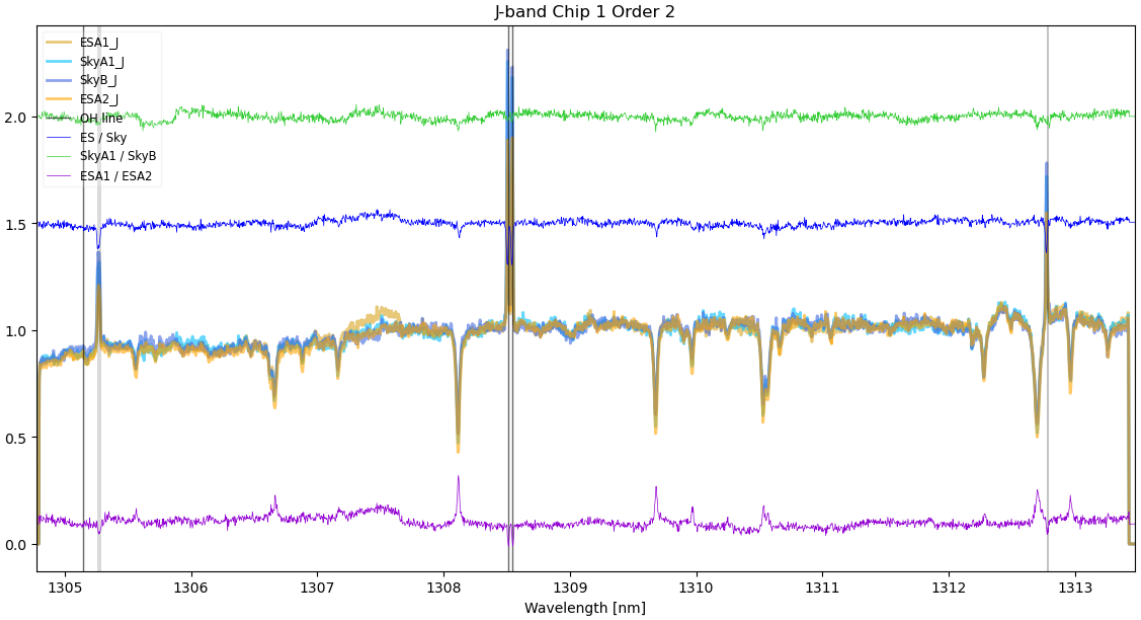

(a) Ratio spectra: ES/Sky (blue), (ESA1/ESA2) (purple), (SkyA1/SkyB) (green). Raw spectra are also shown for completeness, and ratio spectra are vertically shifted for clarity.

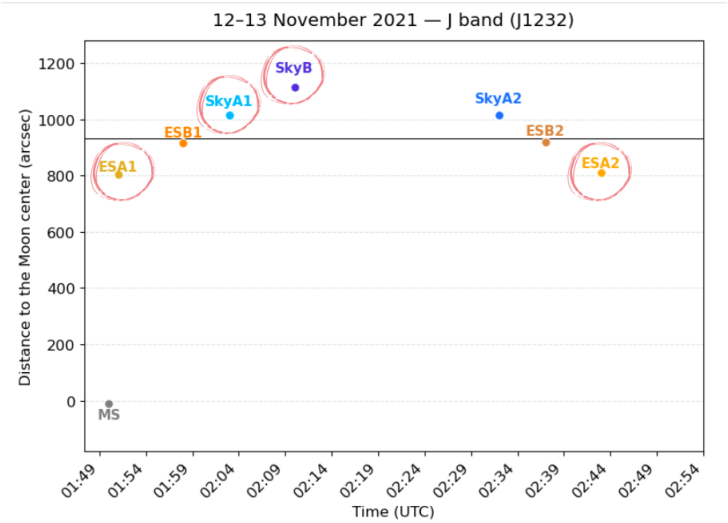

(b) Observation positions for the J-band sequence. Red circles highlight the frames used in the ratio spectra.

Figure 4.6: (a) Ratio spectra. (b) Observation positions.

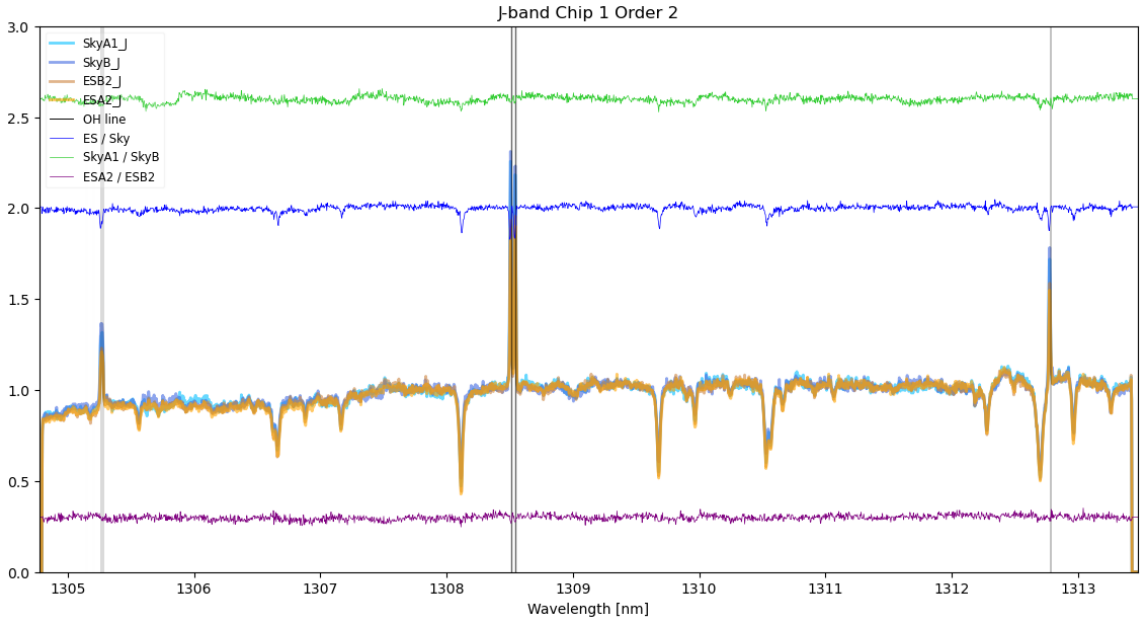

(a) Ratio spectra: ES/Sky (blue), (ESA2/ESB2) (purple), (SkyA1/SkyB) (green). Raw spectra are also shown for completeness, and ratio spectra are vertically shifted for clarity.

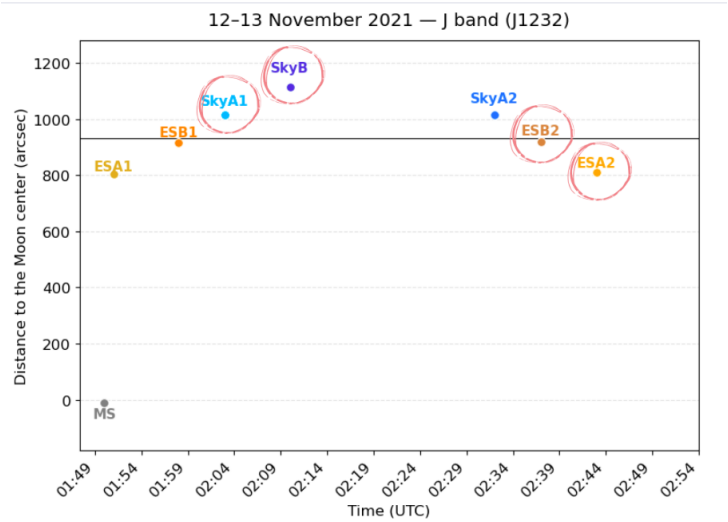

(b) Observation positions for the J-band sequence. Red circles highlight the frames used in the ratio spectra.

Figure 4.7: (a) Ratio spectra. (b) Observation positions.

The same procedure was applied to the H, K, and Y bands. The selected positions and the resulting spectra for these bands are shown in Figs. 4.8, 4.10, and 4.11. While stable, well–constrained ratio spectra were obtained for the H and K bands without any problem, this was not the case for the Y band. Therefore, alternative Earthshine/Sky pairings were tested; an example is shown in Fig. 4.9. However, the Y-band ratios remained inconsistent, and a solution could not be achieved. Why the Y-band results may not be satisfactory is discussed in the Results chapter.

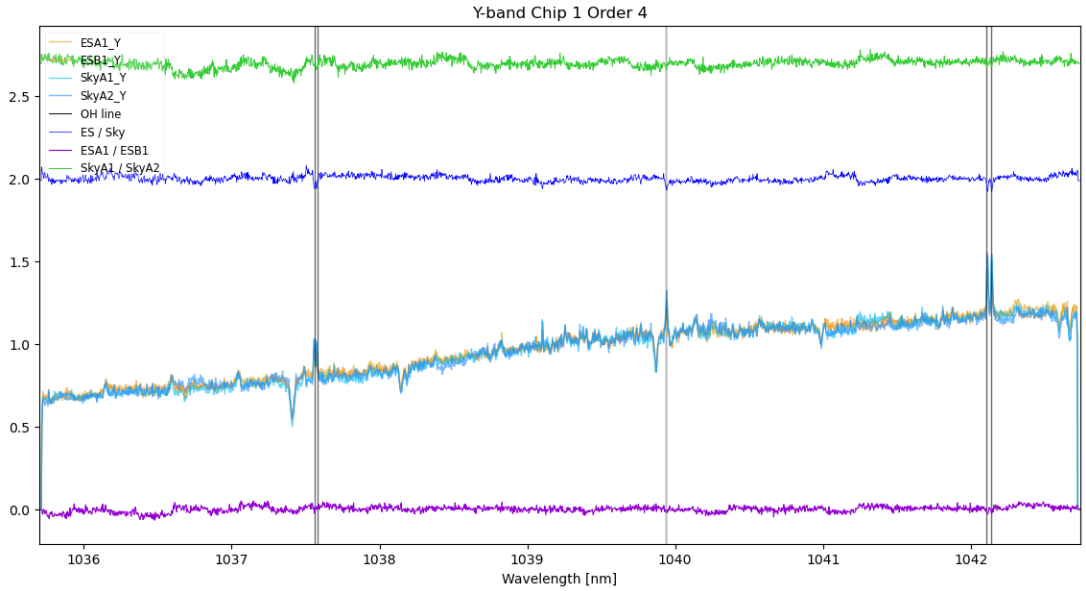

(a) Ratio spectra: ES/Sky (blue), ESA1/ESB1 (purple), SkyA1/SkyA2 (green). Raw spectra are also shown for completeness, and ratio spectra are vertically shifted for clarity.

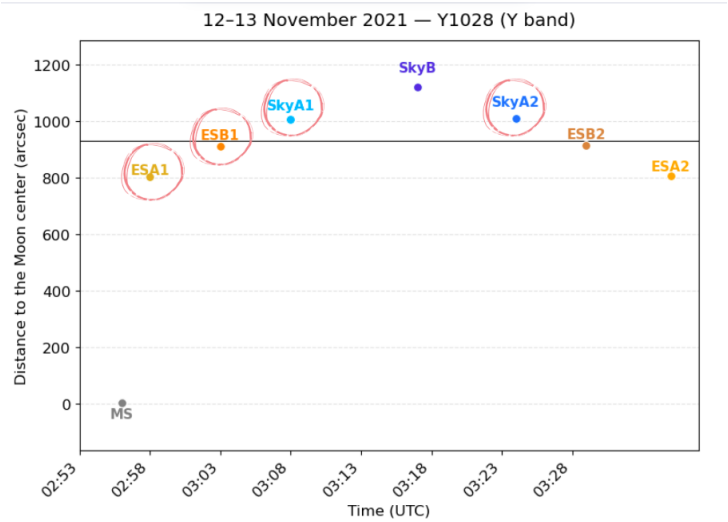

(b) Observation positions for the Y-band sequence. Red circles highlight the frames used in the ratio spectra.

Figure 4.8: (a) Ratio spectra. (b) Observation positions.

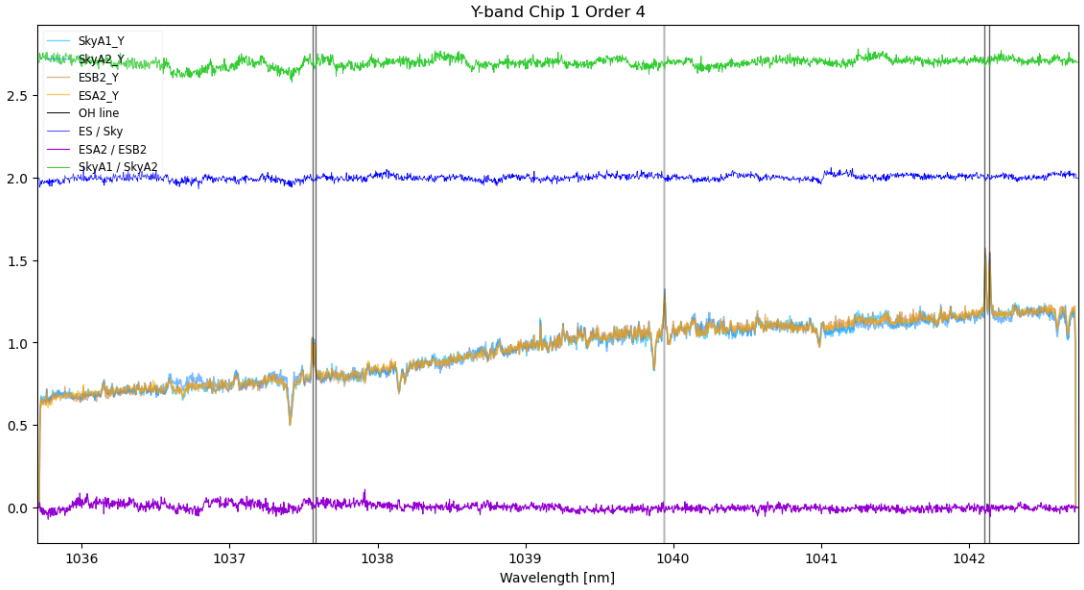

(a) Alternative Ratio spectra: ES/Sky (blue), ESA2/ESB2 (purple), SkyA1/SkyA2 (green). Raw spectra are also shown for completeness, and ratio spectra are vertically shifted for clarity.

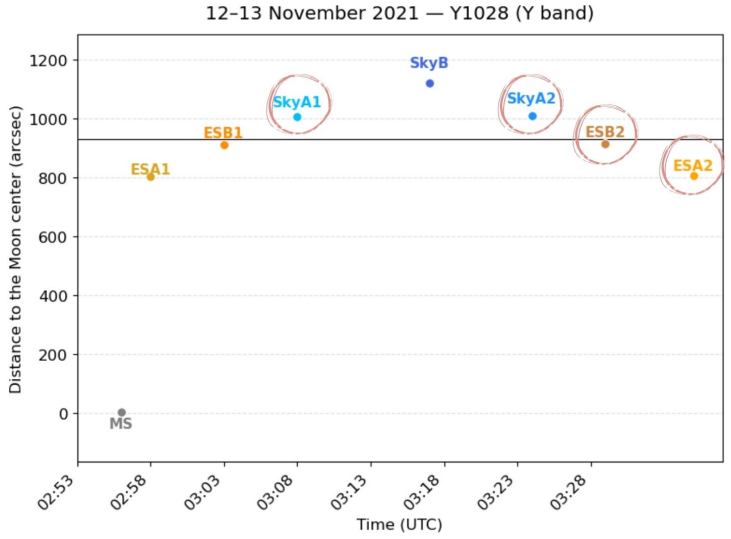

(b) Observation positions for the alternative Y-band sequence. Red circles highlight the frames used in the ratio spectra.

Figure 4.9: (a) Ratio spectra. (b) Observation positions for the alternative Y-band selection.

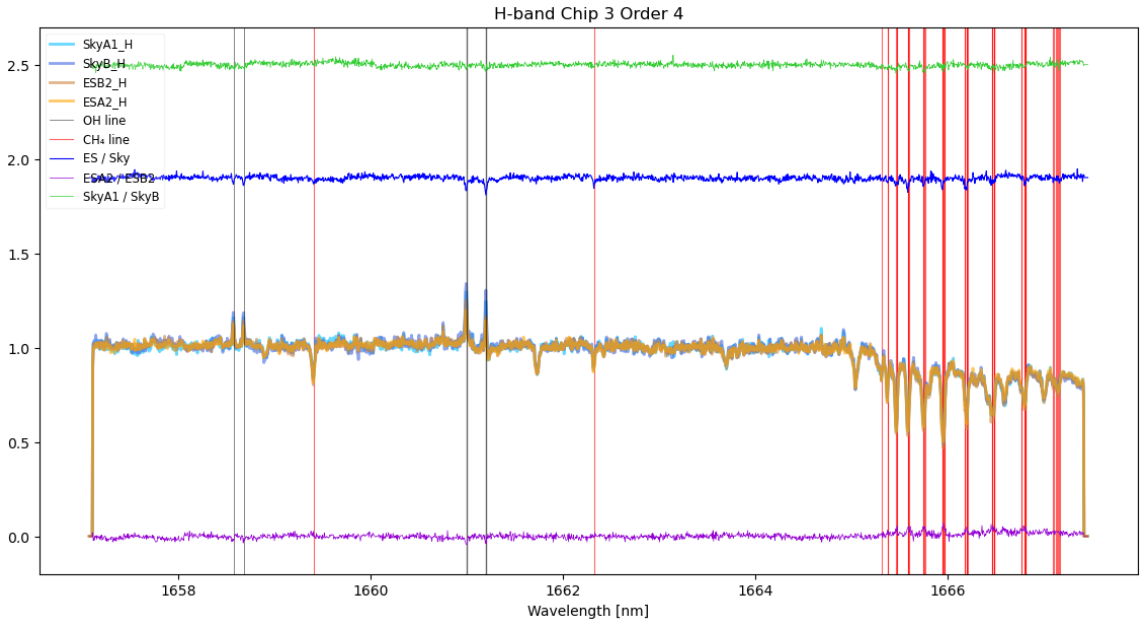

(a) Ratio spectra: ES/Sky (blue), ESB2/ESA2 (purple), SkyA1/SkyB (green). Raw spectra are also shown for completeness, and ratio spectra are vertically shifted for clarity.

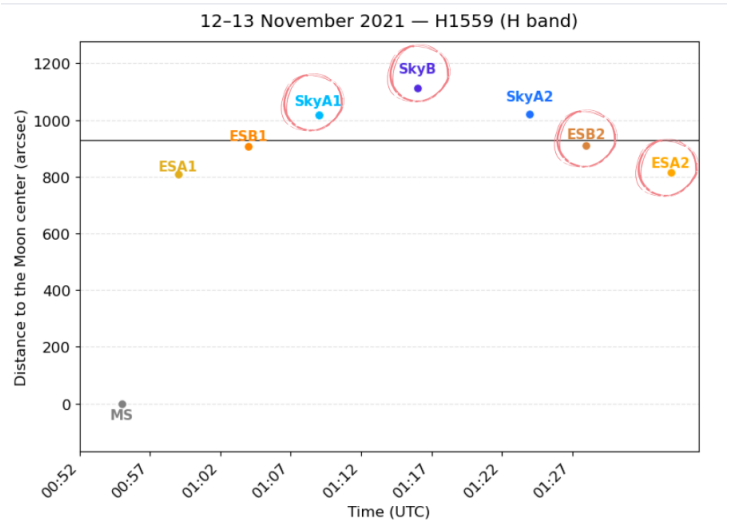

(b) Observation positions for the H-band sequence. Red circles highlight the frames used in the ratio spectra.

Figure 4.10: (a) Ratio spectra. (b) Observation positions.

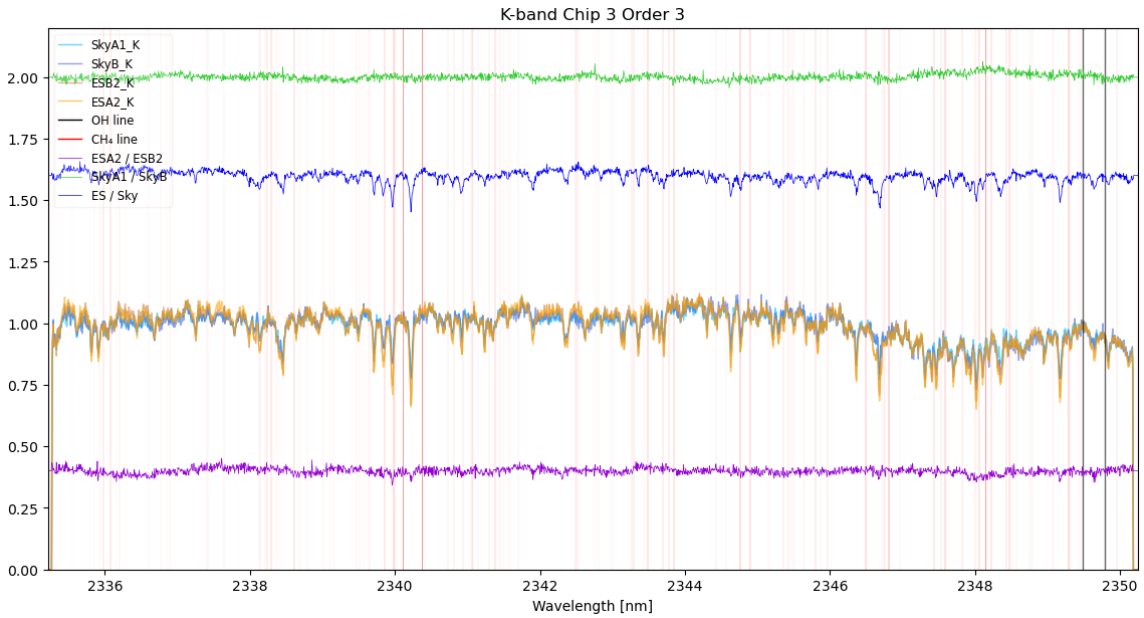

(a) Ratio spectra: ES/Sky (blue), ESB2/ESA2 (purple), SkyA1/SkyB (green). Raw spectra are also shown for completeness, and ratio spectra are vertically shifted for clarity.

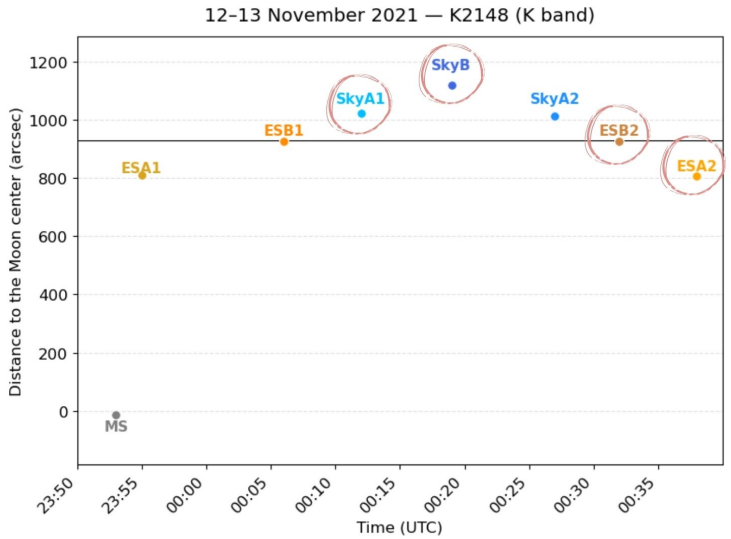

(b) Observation positions for the K-band sequence. Red circles highlight the frames used in the ratio spectra.

Figure 4.11: (a) Ratio spectra. (b) Observation positions.

In Figs. 4.7a, 4.8a, 4.9a, 4.10a, and 4.11a, the vertical lines represent the expected positions of OH (black, solid), O_2 (blue, dashed), and CH_4 (red, solid) transitions overplotted on the ratio spectra. The OH and O_2 lines were taken from the airglow catalog, while the methane transitions were obtained from the HITRAN spectroscopic database [1]. To avoid clutter from negligible features, an intensity cut was applied to the methane catalog lines ($s_w > 1 \times 10^{-22}$), after which the per-species strengths were normalized to the maximum value within the plotted wavelength interval and mapped to the marker thickness. In this way, thicker vertical lines correspond to stronger transitions, allowing the visual impression of line density and strength to be directly linked to the underlying molecular data.

The H band (Fig. 4.10a) is particularly interesting: even after applying the intensity filter, a dense forest of CH_4 lines remains, and many of these red markers coincide with clear absorption structures in ES/Sky, consistent with strong methane absorption in this spectral region.

After this rough line detection analysis, it was required to perform Gaussian fits to the ratio spectra in order to analyze the line identification in more detail. The strength-weighted markers provided a first visual guide to the molecular features, but quantitative fitting was needed to measure their positions, depths, and widths with higher precision. This also allowed a statistical comparison across the different bands and observing positions. The following chapter is therefore devoted to a more detailed description of the fitting procedure and subsequent analysis.

4.3.2 Line Fitting to Ratio Spectra

To extract quantitative information from the ratio spectra, Gaussian absorption profiles were fitted to the candidate lines in the three ratio types: ES/Sky, ES/ES, and Sky/Sky. Each spectrum was saved order by order and chip by chip, and the fits were applied separately for every order on each detector chip.

The first attempt to apply the Gaussian fits used the same routine as for the raw spectra. However, this approach did not succeed, since the ratio spectra are fundamentally different from the raw exposures. In particular, the raw spectra were fitted without normalization, while the ratio spectra were already normalized by construction. As a result, the initial routine returned unstable or unphysical fits.

For this reason, a new fitting procedure was developed for the ratio spectra. In the new approach, the fitting parameters were adapted so that they did not depend on the guess amplitude derived from the local flux range, as was the case for the raw spectra (see Eq.(4.1.2)). Instead, constant parameter bounds and initial values were adopted.

The same Gaussian model used for the raw spectra was adopted for the ratio spectra (see Eq((4.2)). The initial guesses were set as follows: the line width was tied to the instrumental resolution, i.e. $\mathrm{FWHM}_0 = \lambda^*/R$ with $R = 100{,}000$; the amplitude was taken as the local range of the ratio flux within the fitting window, $A_0 = \max(F) - \min(F)$; and the baseline offset was initialized at 0.0. A narrow window was adopted around each candidate wavelength, $[\lambda^* - 0.07\ \mathrm{nm},\ \lambda^* + 0.07\ \mathrm{nm}]$.

Parameter bounds were:

$$\mu \in [\lambda^* - 0.07,\ \lambda^* + 0.07]\ \text{nm},$$

$$\text{FWHM} \in [0.005,\ 0.10]\ \text{nm},$$

$$A \in [0.0,\ 0.5],$$

$$\text{offset} \in [-0.05,\ 0.05].$$

Overall, in the raw spectra, the same Gaussian model was used, but the fits were run with a wider window, the parameter bounds were tied to whatever amplitude the data suggested, and the allowed line widths were fairly loose. For the ratio spectra, the approach was tightened: the bounds were kept fixed (not driven by the local amplitude), and the search was confined to a narrower region around each line.

With these settings, a representative J-band case is shown in Fig. 4.12. The three ratio types are on the same footing, so their parameters can be compared directly. The same workflow was applied to Y, H, and K; only the J-band panel is shown here to keep the presentation compact.

After the ratio–spectrum fits were completed, the line list was broadened beyond OH, O_2, and CH_4 to include H_2O, N_2O, and CO_2 (from HITRAN [1]). For each species, the number of matched lines and their strengths were assessed using the fitted amplitudes as a simple proxy. The full set of plots and the band–by–band comparisons are presented in the Results chapter.

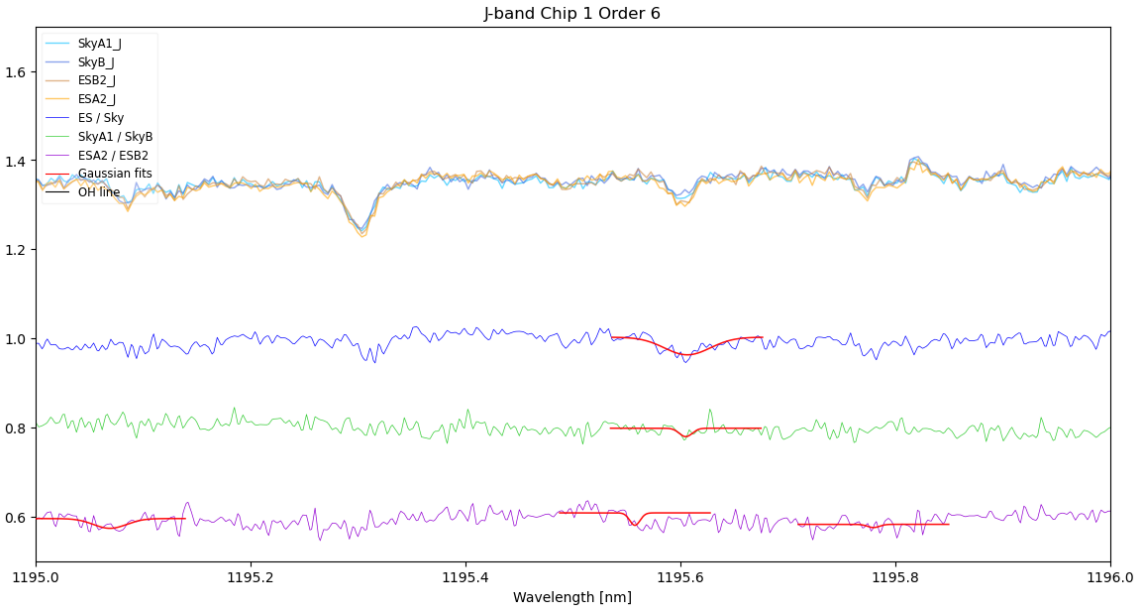

(a) Zoom on J band, chip 1, order 6.

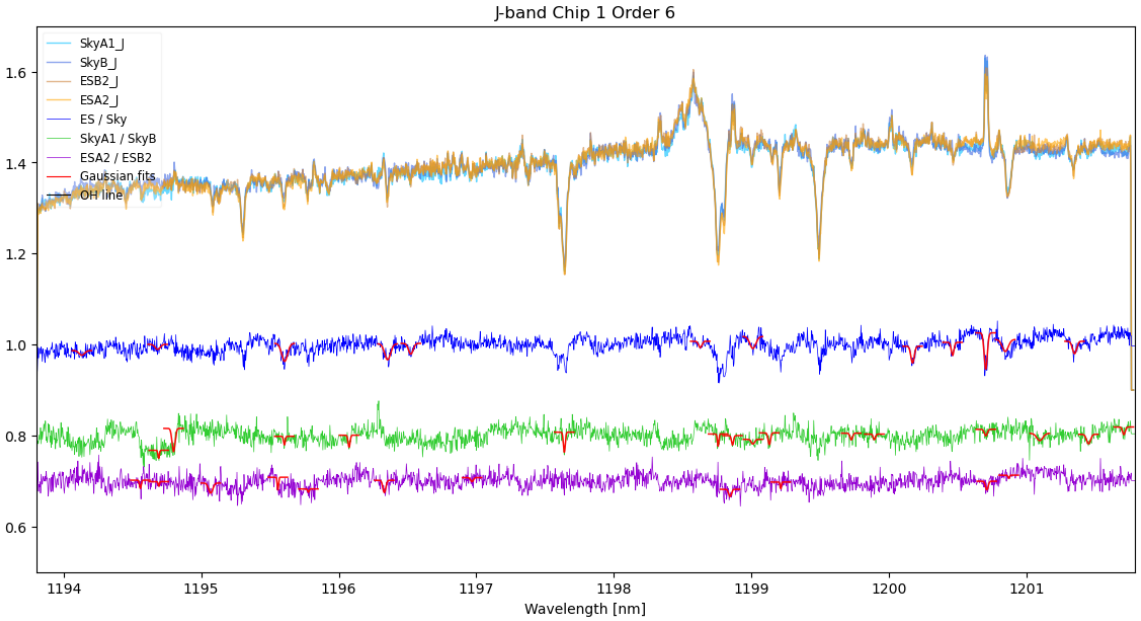

(b) Full spectral range for the same order.

Figure 4.12: Ratio spectra: ES/Sky (blue), SkyA1/SkyB (green), and ESA2/ESB2 (purple). The corresponding raw spectra are overplotted. Red curves show the Gaussian fits to the three ratios. Ratio spectra are vertically shifted for clarity.

Chapter 5

Results

5.1 Molecular Line Identification

After the ratio–fits, the molecule detection was expanded beyond OH, O_2, and CH_4 to include additional telluric species (H_2O, N_2O, CO_2; from HITRAN [1]). Accepted Gaussian fits from the ratio spectra (ES/Sky, ES/ES, Sky/Sky) were then collated order by order and chip by chip. For each fitted feature, the central wavelength, amplitude, and FWHM were retained. In parallel, species line catalogs were assembled. Catalog matching was performed with a tolerance that scales with the fitted width. Concretely, a catalog transition was accepted as a match to a fitted feature if $|\lambda_{\text{fit}} - \lambda_{\text{cat}}| \leq \Delta\lambda_{\text{tol}}$, with $\Delta\lambda_{\text{tol}} \equiv \text{FWHM}_{\text{fit}}$.

Features with no qualifying neighbors in any catalog were collected in an `OTHER`. The results were summarized statistically rather than line–by–line. For each species within the covered interval, the distribution of matched amplitudes was shown as both a histogram and an empirical cumulative distribution.

In Table 5.1, the identified lines in every band are reported. As expected, OH was found mainly in all bands, while CH_4, CO_2, and N_2O were mainly detected in the H and K bands.

Table 5.1: Number of identified molecular lines in each band and dataset.

Dataset	O_2	OH	CH_4	H_2O	CO_2	N_2O	O_2	OH	CH_4	H_2O	CO_2	N_2O
			Y band						**H band**			
ES/Sky	–	60	–	1	–	–	12	82	49	13	31	20
ES/ES	–	47	–	6	–	–	13	67	21	0	13	7
Sky/Sky	–	56	–	–	–	–	7	66	28	8	13	13
			J band						**K band**			
ES/Sky	74	65	2	32	–	–	–	25	231	29	56	54
ES/ES	65	41	1	34	–	–	–	16	126	33	3	45
Sky/Sky	50	36	1	34	–	–	–	23	178	29	6	44

5.2 Amplitude distributions of detected lines

The line identification showed that several molecules could be detected in the Earthshine spectra. After this step, the statistical analysis of the amplitude distributions of the detected lines was carried out. Figures 5.1, 5.2, 5.4 5.5, and 5.6 present the distributions for the Y, J, H, and K bands. Panels (a), (b), and (c) show the ratio spectra separately, while panel (d) shows the overlay that makes it possible to compare the distributions fairly. Alongside each species label in the legends, a matched counter reported how many fitted features were associated with that species over how many catalog transitions fell inside the wavelength range.

It can be seen from the figures that the amplitude of the ES/Sky spectra consistently follows the same trend: it is systematically higher than both ES/ES and Sky/Sky. This finding suggests that the Earthshine signal is indeed present. However, this trend does not hold for the Y band. As mentioned before, even though multiple alternative exposure pairs were tested, no successful result was obtained. From the Y band plots, it can be seen that the ES/Sky amplitudes, which are expected to be higher than those of ES/ES and Sky/Sky, never reached that level. Figure 5.2 shows an alternative selection of exposure pairs (ESA2 and ESB2), but in this case, the situation is even worse than in Fig. 5.1: while in the first case at least the OH lines had higher amplitudes in ES/Sky compared to ES/ES and Sky/Sky, in the alternative scenario both the OH and the other molecular lines show lower amplitudes.

Another pair that was tested was ESA1 and ESA2 for the Y band. Even though these exposures have approximately a 30-minute observation difference, they were still worth testing since they correspond to the closest part of the Moon center. The idea was that ESB1 and ESB2, being closer to the lunar edge, might not represent pure Earthshine but rather include more sky contribution. However, after testing the ESA1 and ESA2 pair, the outcome remained the same: the ES/Sky amplitudes were still lower than those of ES/ES and Sky/Sky. Thus, no improvement compared to the previous selection. Figure 5.3 shows the result of this analysis. The individual plots are not included here, since the overlay view already shows the main differences between the three datasets.

Even though the Y band was first included in the analysis, the results showed that it is not suitable for a reliable comparison. The Y-band spectra contain only a few telluric absorption lines, and the signal is much weaker than in the other near-infrared bands. Also, the Moonshine contribution is stronger at shorter wavelengths, which can hide or reduce the already faint Earthshine signal. In addition, small guiding or alignment errors during the observations may have affected the flux stability in the Y band more strongly than in the other bands.

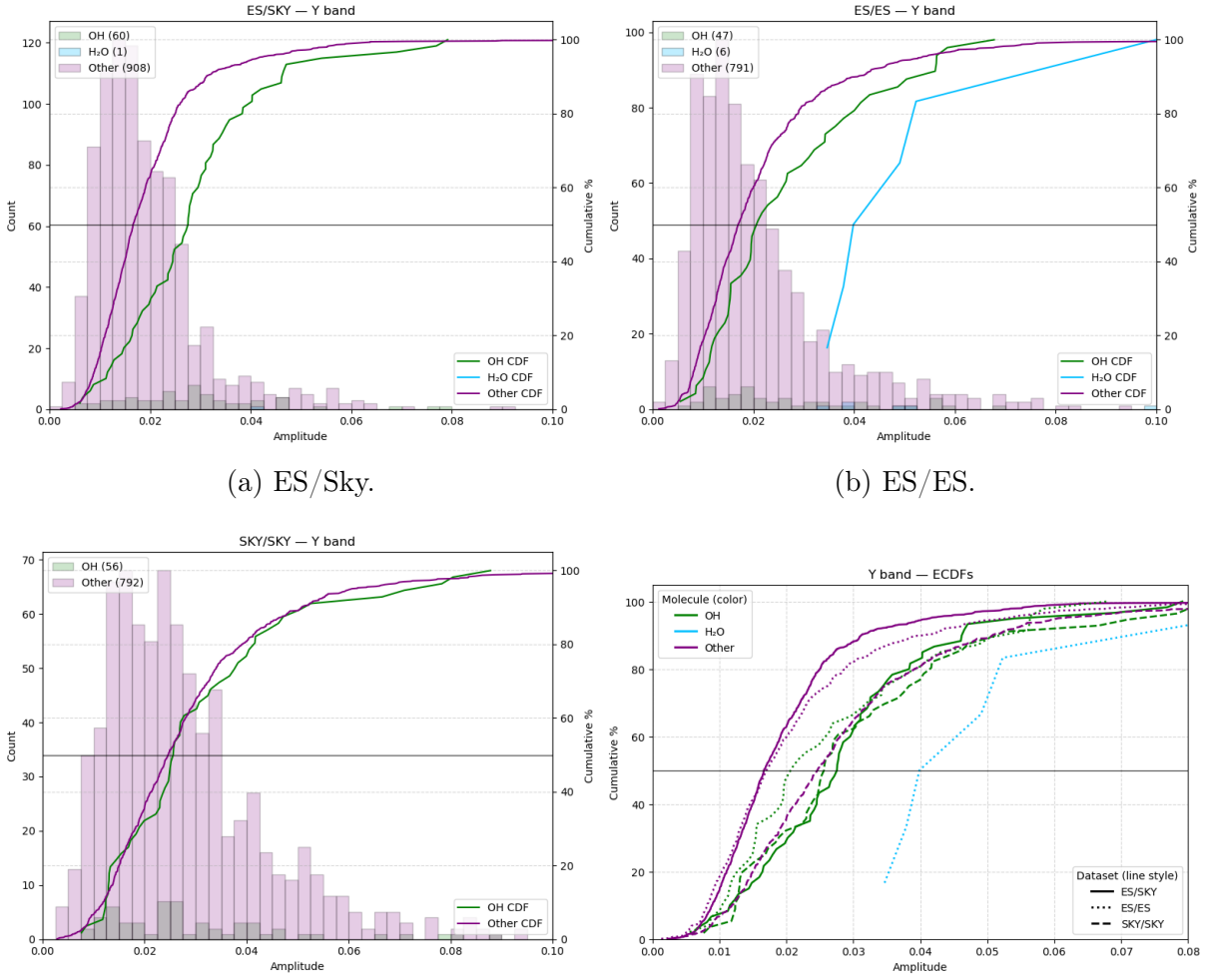

(a) ES/Sky.

(b) ES/ES.

(c) Sky/Sky.

(d) Overlay of all three ratios (ECDFs).

Figure 5.1: Y band amplitude distributions: histograms with ECDFs by molecule. In panel (d), ECDFs are overlaid for the three ratios (solid: ES/Sky; dotted: ES/ES; dashed: Sky/Sky). Colors indicate species.

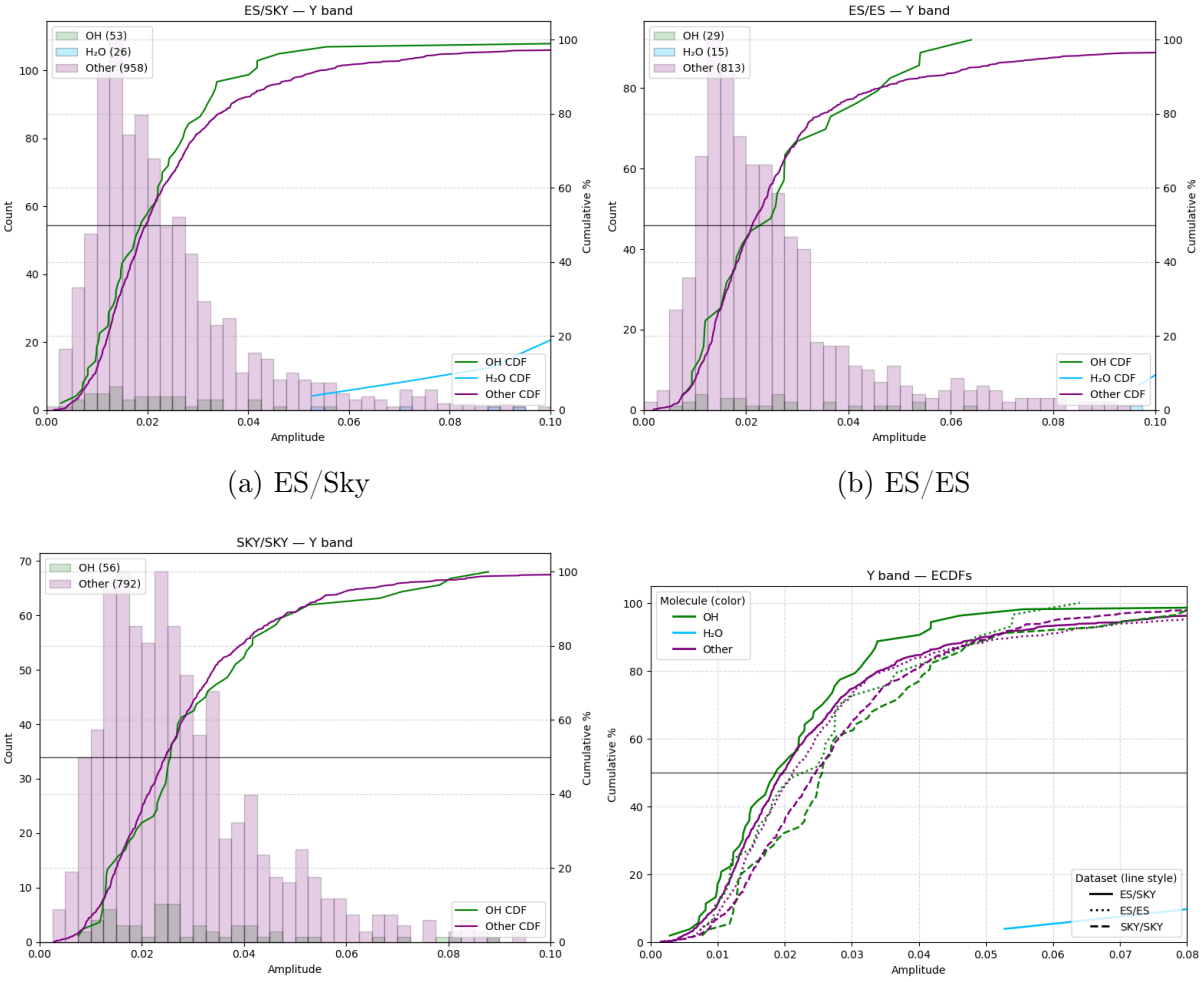

(a) ES/Sky

(b) ES/ES

(c) Sky/Sky

(d) Overlay of all three ratios for comparison.

Figure 5.2: Y band alternative exposure pair (ESA2 and ESB2) amplitude distributions: histograms with ECDFs by molecule. In panel (d), ECDFs are overlaid for the three ratios (solid: ES/Sky; dotted: ES/ES; dashed: Sky/Sky). Colors indicate species.

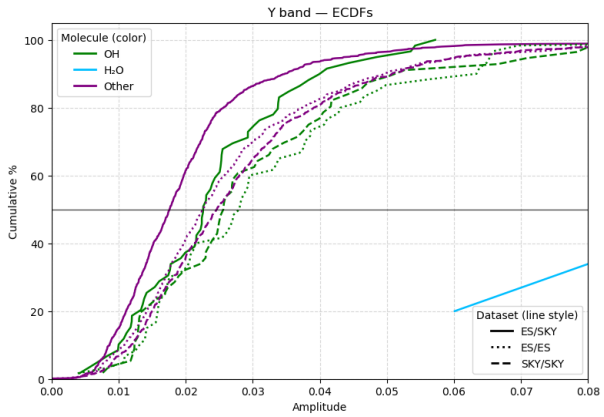

Figure 5.3: Y band overlay comparison for the alternative exposure pair (ESA1 and ESA2). Only the overlay analysis is shown for compactness.

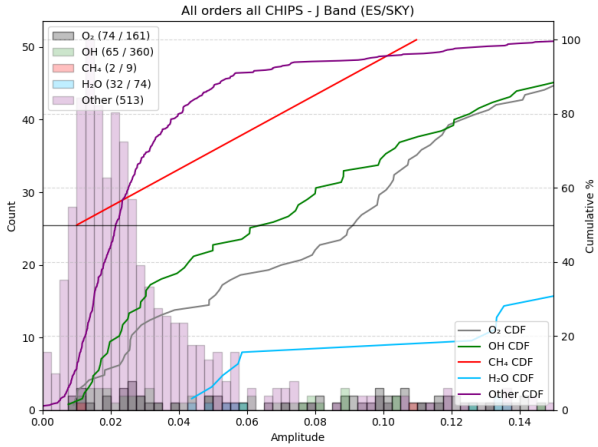

(a) ES/Sky.

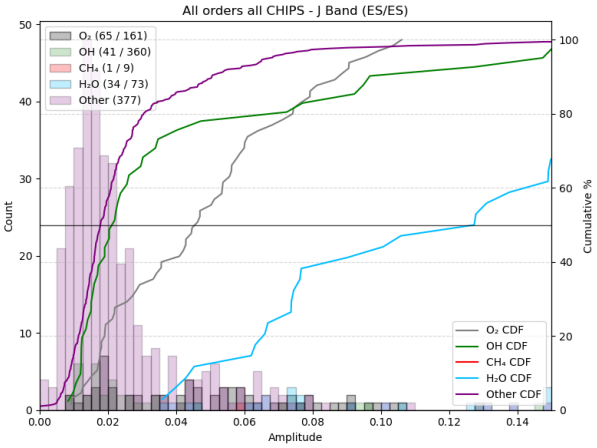

(b) ES/ES.

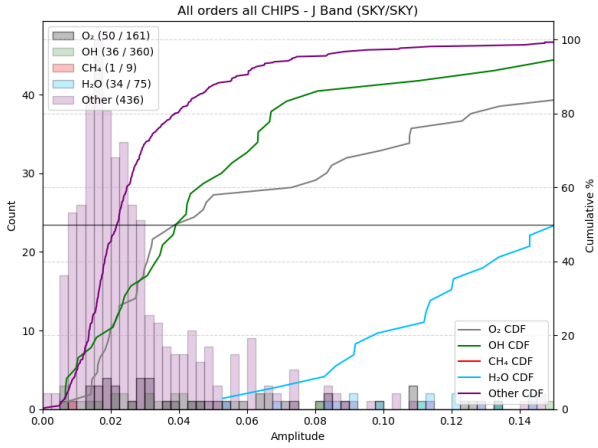

(c) Sky/Sky.

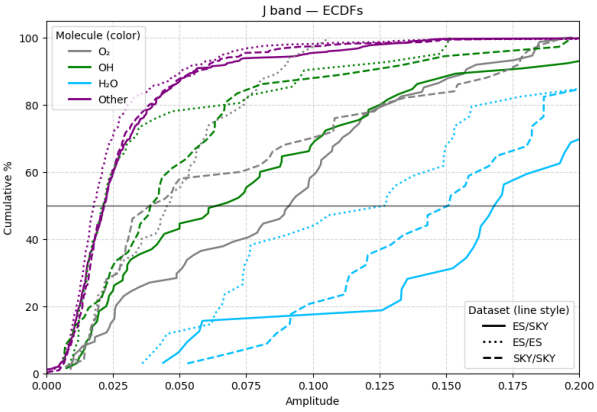

(d) Overlay of all three ratios (ECDFs).

Figure 5.4: J band amplitude distributions: histograms with ECDFs by molecule. In panel (a), ECDFs are overlaid for the three ratios (solid: ES/Sky; dotted: ES/ES; dashed: Sky/Sky). Colors indicate species.

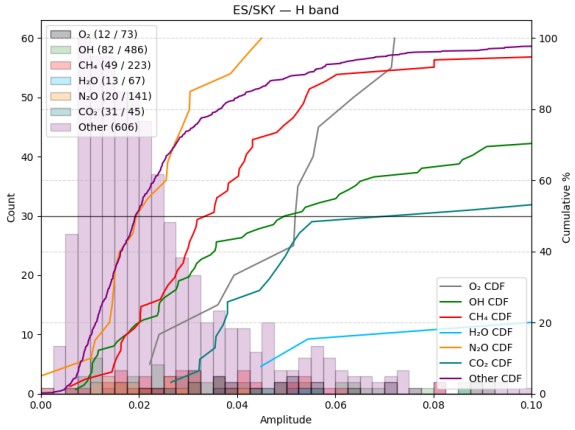

(a) ES/Sky

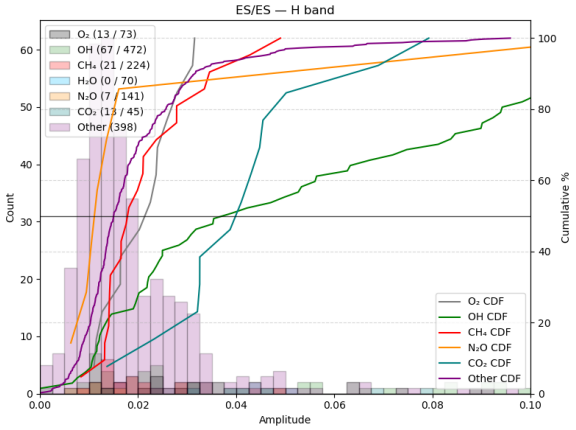

(b) ES/ES

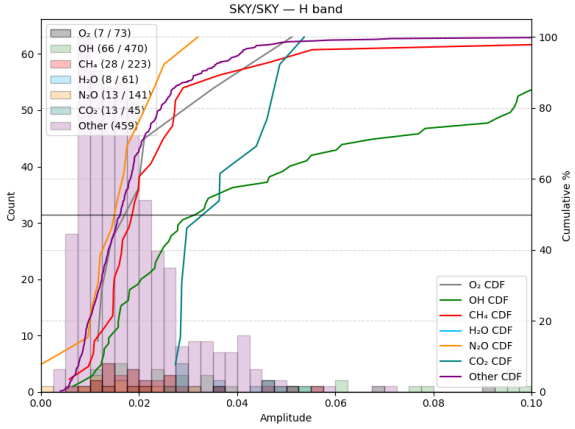

(c) Sky/Sky

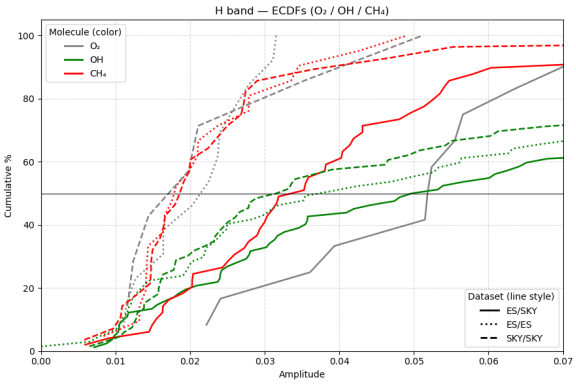

(d) ECDF overlay: O_2, OH, CH_4 (solid = ES/Sky; dotted = ES/ES; dashed = Sky/Sky).

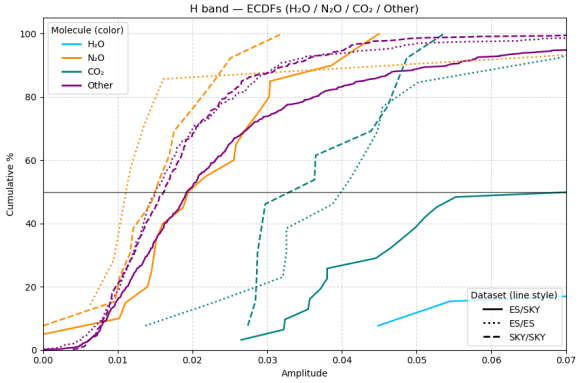

(e) ECDF overlay: H_2O, N_2O, CO_2, `Other` (same line styles).

Figure 5.5: H band amplitude distributions. Panels (a)–(c): each dataset shown as histogram with ECDFs by molecule. (d)–(e): ECDF-only overlays split by molecule groups for readability (datasets distinguished by line style: solid = ES/Sky; dotted = ES/ES; dashed = Sky/Sky).

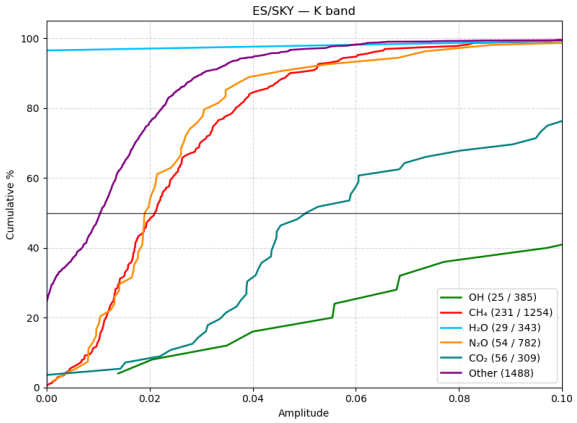

(a) ES/Sky

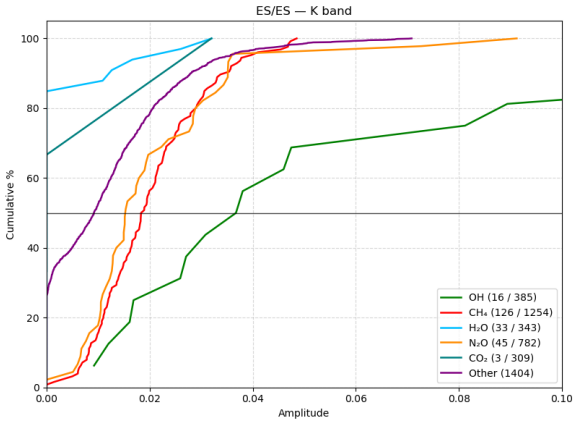

(b) ES/ES

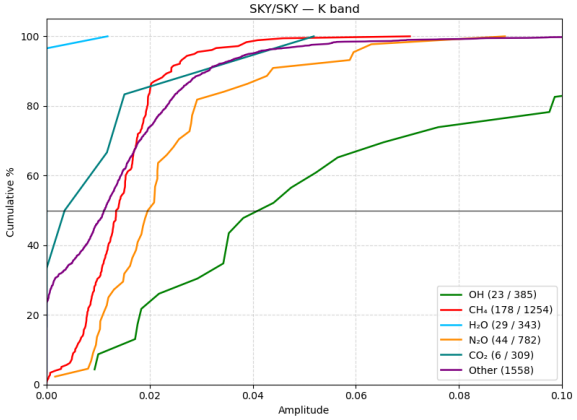

(c) Sky/Sky

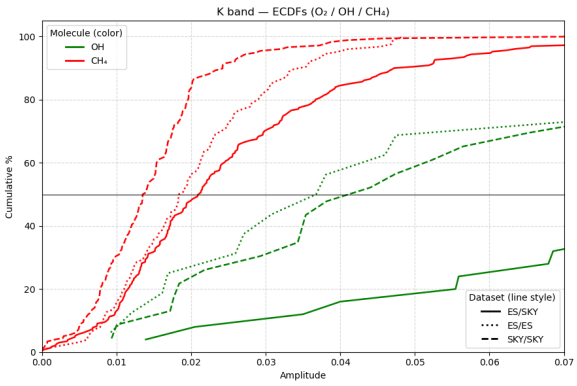

(d) ECDF overlay: O_2, OH, CH_4 (solid = ES/Sky; dotted = ES/ES; dashed = Sky/Sky).

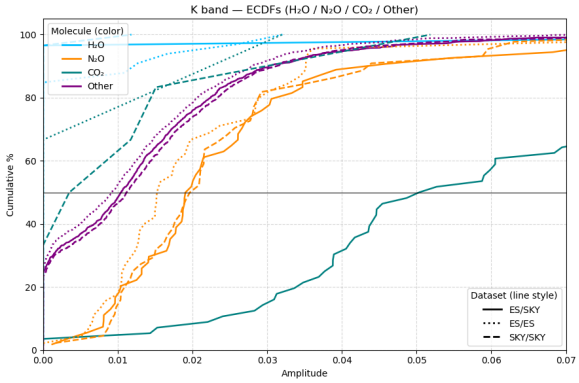

(e) ECDF overlay: H_2O, N_2O, CO_2, `Other` (same line styles).

Figure 5.6: K band amplitude distributions. Panels (a)–(c): each dataset shown as histogram with ECDFs by molecule. Panels (d)–(e): ECDF-only overlays split into molecule groups for readability (datasets distinguished by line style: solid = ES/Sky; dotted = ES/ES; dashed = Sky/Sky).

5.3 Distributional comparisons via Anderson–Darling and Kolmogorov–Smirnov tests

After inspecting the empirical cumulative distributions of the line amplitudes, it was evident that the ES/Sky ratios systematically showed stronger absorption than both ES/ES and Sky/Sky. However, visual inspection alone is not sufficient to establish whether these differences are statistically significant. For this reason, a quantitative comparison of the amplitude distributions was done by two tests: the Kolmogorov–Smirnov (KS) test and the Anderson–Darling k–sample test. These tests check whether two samples come from the same distribution. Both start with the same idea; the null hypothesis, which means we first assume that the samples are from the same population. Then, depending on the p-value, we decide if we keep or reject this assumption. The p-value is defined as "the smallest level of significance that would lead to rejection of the null hypothesis (H_0) with the given data." [47] Therefore, it is necessary to set a threshold for the p-value, called the significance level. In this analysis, the significance level was chosen as 0.05.

In the Anderson–Darling a larger A^2 value indicates that the distributions are more different, whereas smaller or even negative values indicate that they are more alike [3], [2]. Similarly, in the Kolmogorov–Smirnov (KS) test, the test statistic KS ranges from 0 to 1 and it represents the maximum absolute difference between the cumulative distribution functions of the two samples. [10] Values of KS closer to 1 indicate a large differences between the distributions, while values near 0 imply strong similarity. As with the Anderson–Darling test, the associated p-value is used to assess whether the observed difference is statistically significant.

In this work, the expectation was that the ES/Sky comparisons would yield large A^2 values together with small p-values, consistent with the stronger absorption seen in Earthshine. On the other hand, comparisons between ES/ES and Sky/Sky were expected to give smaller or negative A^2 values with higher p-values, which would show the similarity between the two datasets, as they both represent the noise. The same trend was expected from the Kolmogorov–Smirnov (KS) test: larger KS values and correspondingly low p-values for ES/Sky, greater differences between the distributions, and smaller KS values with higher p-values for ES/ES and Sky/Sky, consistent with their closer agreement.

The following tables (Tables 5.2, 5.3, 5.4, and 5.5) present the raw results of the Anderson–Darling and Kolmogorov–Smirnov tests. In these tables, p-values smaller than the chosen significance level of 0.05 are shown in bold. The bold results indicate that the null hypothesis can be rejected. Therefore, the compared samples come from different distributions. Some important results of these tests are discussed further below.

Even though it was already visible from the plots that the amplitudes in the Y band behaved abnormally, with the ES/SKY amplitudes being lower than both ES/ES and SKY/SKY, it was still worth checking the statistical results. Table 5.2 shows that in the Y band, only the OH and Other categories were detected. All OH distributions appear similar to each other, and all other group distributions show the same behaviour across datasets. This further confirms that the Y-band analysis does not provide reliable information. As a result, the amplitude distributions and ratio spectra in this band do not show clear molecular patterns, and no significant differences were found between the Earthshine and Sky data. Therefore, the Y band was excluded from the main analysis, and the focus was placed on the J, H, and K bands.

Table 5.2: Anderson–Darling (AD) and Kolmogorov–Smirnov (KS) tests for Y band amplitude distributions. Boldface indicates $p < 0.05$.

Molecule	Comparison	A^2	p	KS	p	(n_1, n_2)
OH	ES/SKY vs ES/ES	0.526	0.201	0.220	0.130	(60, 47)
	ES/SKY vs SKY/SKY	-0.680	0.250	0.123	0.718	(60, 56)
	ES/ES vs SKY/SKY	0.185	0.250	0.214	0.161	(47, 56)
Other	ES/SKY vs ES/ES	4.632	**0.00471**	0.084	**0.00508**	(908, 791)
	ES/SKY vs SKY/SKY	117.530	**0.001**	0.300	$\mathbf{4.24 \times 10^{-34}}$	(908, 792)
	ES/ES vs SKY/SKY	78.099	**0.001**	0.251	$\mathbf{2.81 \times 10^{-22}}$	(791, 792)

Table 5.3: Anderson–Darling (AD) and Kolmogorov–Smirnov (KS) tests for J band amplitude distributions. Boldface indicates $p < 0.05$.

Molecule	Comparison	A^2	p	KS	p	(n_1, n_2)
O_2	ES/SKY vs ES/ES	15.391	**0.001**	0.452	$\mathbf{6.34 \times 10^{-7}}$	(74, 65)
	ES/SKY vs SKY/SKY	1.950	0.0511	0.290	**0.010**	(74, 50)
	ES/ES vs SKY/SKY	3.629	**0.0111**	0.300	**0.0094**	(65, 50)
OH	ES/SKY vs ES/ES	8.844	**0.001**	0.393	$\mathbf{5.31 \times 10^{-4}}$	(65, 41)
	ES/SKY vs SKY/SKY	2.323	**0.0361**	0.326	**0.0106**	(65, 36)
	ES/ES vs SKY/SKY	2.647	**0.0268**	0.350	**0.0132**	(41, 36)
H_2O	ES/SKY vs ES/ES	4.588	**0.00489**	0.450	**0.0016**	(32, 34)
	ES/SKY vs SKY/SKY	1.084	0.117	0.248	0.215	(32, 34)
	ES/ES vs SKY/SKY	2.581	**0.0285**	0.324	0.0564	(34, 34)
Other	ES/SKY vs ES/ES	7.153	**0.001**	0.139	$\mathbf{3.78 \times 10^{-4}}$	(513, 377)
	ES/SKY vs SKY/SKY	-0.272	0.250	0.064	0.278	(513, 436)
	ES/ES vs SKY/SKY	8.422	**0.001**	0.143	$\mathbf{4.64 \times 10^{-4}}$	(377, 436)

Table 5.4: Anderson–Darling (AD) and Kolmogorov–Smirnov (KS) tests for H band amplitude distributions. Boldface indicates $p < 0.05$.

Molecule	Comparison	A^2	p	KS	p	(n_1, n_2)
O_2	ES/SKY vs ES/ES	8.761	**0.001**	0.833	$\mathbf{1.15 \times 10^{-4}}$	(12, 13)
	ES/SKY vs SKY/SKY	6.055	**0.00148**	0.714	**0.00976**	(12, 7)
	ES/ES vs SKY/SKY	-0.355	0.250	0.286	0.734	(13, 7)
OH	ES/SKY vs ES/ES	1.526	0.0762	0.180	0.155	(82, 67)
	ES/SKY vs SKY/SKY	2.682	**0.026**	0.192	0.114	(82, 66)
	ES/ES vs SKY/SKY	-0.691	0.250	0.104	0.805	(67, 66)
CH_4	ES/SKY vs ES/ES	7.457	**0.001**	0.469	**0.00192**	(49, 21)
	ES/SKY vs SKY/SKY	8.485	**0.001**	0.495	$\mathbf{1.74 \times 10^{-4}}$	(49, 28)
	ES/ES vs SKY/SKY	-0.957	0.250	0.155	0.900	(21, 28)
N_2O	ES/SKY vs ES/ES	1.928	0.0521	0.564	**0.0434**	(20, 7)
	ES/SKY vs SKY/SKY	0.761	0.160	0.373	0.161	(20, 13)
	ES/ES vs SKY/SKY	-0.304	0.250	0.330	0.588	(7, 13)
CO_2	ES/SKY vs ES/ES	4.727	**0.00435**	0.516	**0.00891**	(31, 13)
	ES/SKY vs SKY/SKY	7.248	**0.001**	0.568	**0.00283**	(31, 13)
	ES/ES vs SKY/SKY	-0.323	0.250	0.308	0.588	(13, 13)
Other	ES/SKY vs ES/ES	22.082	**0.001**	0.201	$\mathbf{5.61 \times 10^{-9}}$	(606, 398)
	ES/SKY vs SKY/SKY	23.320	**0.001**	0.179	$\mathbf{9.16 \times 10^{-8}}$	(606, 459)
	ES/ES vs SKY/SKY	0.031	0.250	0.055	0.511	(398, 459)

Table 5.5: Anderson–Darling (AD) and Kolmogorov–Smirnov (KS) tests for K band amplitude distributions. Boldface indicates $p < 0.05$.

Molecule	Comparison	A^2	p	KS	p	(n_1, n_2)
OH	ES/SKY vs ES/ES	5.117	**0.00315**	0.527	**0.00522**	(25, 16)
	ES/SKY vs SKY/SKY	6.276	**0.00124**	0.456	**0.00912**	(25, 23)
	ES/ES vs SKY/SKY	-0.904	0.250	0.163	0.915	(16, 23)
CH_4	ES/SKY vs ES/ES	3.030	**0.019**	0.139	0.0763	(231, 126)
	ES/SKY vs SKY/SKY	32.260	**0.001**	0.380	$\mathbf{1.69 \times 10^{-13}}$	(231, 178)
	ES/ES vs SKY/SKY	15.498	**0.001**	0.302	$\mathbf{1.91 \times 10^{-6}}$	(126, 178)
H_2O	ES/SKY vs ES/ES	0.455	0.216	0.117	0.958	(29, 33)
	ES/SKY vs SKY/SKY	-1.328	0.250	0.034	1.000	(29, 29)
	ES/ES vs SKY/SKY	0.626	0.182	0.121	0.944	(33, 29)
N_2O	ES/SKY vs ES/ES	0.369	0.235	0.237	0.107	(54, 45)
	ES/SKY vs SKY/SKY	-1.073	0.250	0.077	0.995	(54, 44)
	ES/ES vs SKY/SKY	0.234	0.250	0.215	0.207	(45, 44)
CO_2	ES/SKY vs ES/ES	5.124	**0.00313**	0.821	**0.0176**	(56, 3)
	ES/SKY vs SKY/SKY	7.895	**0.001**	0.780	**0.000684**	(56, 6)
	ES/ES vs SKY/SKY	-0.832	0.250	0.333	0.988	(3, 6)
Other	ES/SKY vs ES/ES	2.722	**0.025**	0.048	0.0733	(1488, 1404)
	ES/SKY vs SKY/SKY	0.016	0.250	0.037	0.233	(1488, 1558)
	ES/ES vs SKY/SKY	7.754	**0.001**	0.069	**0.00162**	(1404, 1558)

5.3.1 Results and interpretation of the statistical tests

As discussed above, the expectation from the ES/Sky, ES/ES, and Sky/Sky distributions is that ES/Sky should differ from the other two in order to indicate the presence of a signal. The results of the tests are shown only for the cases that met the criteria. To ensure reliability, the criterion was made strict: a case was considered significant only if it passed both the Kolmogorov–Smirnov (KS) and Anderson–Darling (AD) tests. The same criterion was also applied to the ES/ES and Sky/Sky comparisons to confirm that these internal consistency checks do not show significant differences, as they are expected to represent similar noise behavior rather than an atmospheric signal.

Table 5.6: Molecules that pass both criteria.

Band	**Molecules**
H	O_2, CH_4, CO_2, `Other`
K	OH, CO_2

The applied criteria are summarized in Table 5.6. The molecules listed in the table are therefore those for which both tests consistently indicate that the ES/Sky distributions are statistically different from the reference ones. This means that these species show a statistically significant Earthshine signal.

While CO_2 and OH are not considered biosignatures, O_2 and CH_4 are among the most promising ones, especially when they are detected together. The simultaneous presence of oxygen and methane in a planetary atmosphere is of particular interest, since these two gases are chemically unstable when coexisting and would quickly react to form CO_2 and H_2O in the absence of continuous replenishment. In this sense, detecting both O_2 and CH_4 in the Earthshine spectrum indicates that the method is sensitive to potential biosignature pairs, and that the observational approach is capable of identifying such combinations in exoplanetary contexts as well.

Although this work is based on statistical comparisons instead of detailed line-by-line modeling, it still provides a useful diagnostic for future studies. For exoplanet observations, the analysis will need to be more advanced, with each absorption line modeled and fitted individually to the data. Still, the methods used here show that it is possible to detect and confirm important molecular features in reflected light, which can help in developing similar techniques for future habitable exoplanet research.

5.4 Model–observation comparison

In order to place the observed Earthshine spectra in a broader context, a qualitative comparison with synthetic radiative transfer simulations was performed. For this purpose, line positions were compared with line-by-line models, and radiative–transfer simulations kindly provided by Claudia Emde[15, 17]. The simulations were done using the MYSTIC Monte Carlo code [41],[15], which is part of the libRadtran radiative transfer library [42], [16]. Earthshine simulations contain five main configurations: Earthshine clear, Earthshine cloud, Sky clear, Sky aerosol, and Moonshine. However, in this work, only Earthshine clear, Earthshine cloud, and Sky clear are used for comparison. For context, the simulations comprised (i) Earthshine for a phase angle of 110° using a mid–latitude summer atmosphere over an ocean surface (wind $10\,\mathrm{m\,s^{-1}}$), and a cloudy case with a homogeneous cloud layer of optical thickness 5; the radiance reaching the Moon was multiplied by a lunar albedo of 0.2; (ii) Moonshine as direct transmission from the top of atmosphere to Paranal (solar zenith angle 35°) scaled by the lunar albedo; and (iii) Sky radiance at Paranal altitude (2635 m) for both clear–sky and an aerosol case including a desert aerosol with optical thickness 0.1. The original results of these simulations are presented in the Appendix (see Fig. A.5).

Before starting the comparison, the simulated spectra were convolved to match the lower spectral resolution of the observations. This step was necessary because the synthetic spectra were originally produced at a much higher resolution. To do this, a Gaussian broadening was applied to the simulated spectra. After this correction, both spectra had comparable resolution, allowing a direct and fair comparison.

First, the raw spectra from the simulations were compared with the raw observational spectra, and then the ratio spectra were compared. For each molecule, the observed ES/Sky ratio was compared with two modeled ratios: ESclear/Skyclear and EScloud/Skyclear. With this approach, atmospheric conditions, such as the effect of clouds presence on the absorption structure, can be analyzed.

The following figures 5.7 5.8, 5.9 show the comparisons for three molecular regions. In the model spectra, the Earthshine clear and Earthshine cloudy cases show clear differences in line depth. The absorption lines are deeper in the clear-sky model, because in the cloudy case the light is mostly reflected from the upper parts of the clouds. This means it does not travel through the full atmosphere below the clouds, so part of the absorption is avoided. As a result, the molecular lines appear weaker in the cloudy model compared to the clear case. This difference helps to understand how clouds can change the strength of molecular lines in reflected light. It is worth noting that clouds do not affect all molecular features in the same way; for example, H_2O lines are more strongly affected by clouds than O_2 [57].

Figure 5.7 shows the comparison for the O_2 region near 1266 nm. The raw spectra look quite similar to the model. However, in the ratio spectra, both absorption and apparent emission features appear in the observations, whereas the model shows only absorption features. The right-hand O_2 absorption line matches the model well, while the left-hand line looks like an emission instead. This happens because the line is saturated. When a line is saturated, both the Earthshine and Sky spectra drop close to zero at the line center. If the Sky absorption is just a bit deeper, the ratio (ES/Sky) becomes slightly greater than one, which looks like an emission feature. However, this is not a real physical emission; it's only a mathematical effect caused by the division of two very deep absorption lines.

Figure 5.8 shows the comparison for the CH_4 region near 1640 nm. The overall line positions and shapes in the observed spectra are roughly consistent with the model. The ratio spectra show absorption features that can be recognized in both the clear and cloudy Earthshine simulations, although in the observations the features are weaker and less well defined. The cloudy model gives a slightly better match to the observed ratio, as it predicts shallower features similar to those seen in the data. CH_4 lines do not reach saturation like the strong O_2 lines, since CH_4 is much less abundant in the atmosphere.

It is important to note that the cloud models used in this work assume a homogeneous cloud layer, while in reality clouds are far more complex and unevenly distributed. Roccetti et al.[57] presents the first study that simulates high resolution Earthshine spectra, exploring in detail the role of cloud modelling. They present four different scenarios of cloud structure: (i) a uniform layer, (ii) patchy liquid-water (LW) clouds, (iii) patchy liquid- and ice-water (LW + IW) clouds, and (iv) a fully Earth-like model that includes realistic 3D cloud fields. Their results show that how clouds are modeled has a big effect on the continuum and on the depth of absorption lines like O_2 and H_2O. Simple homogeneous models usually make the absorption lines look deeper than they really are, while more realistic 3D clouds give lower values but a truer picture of how Earth's atmosphere reflects light. Therefore, the comparisons presented in this thesis work should be regarded as qualitative, while more realistic interpretations would require the use of full 3D cloud simulations such as those developed by Roccetti et al. [57].

Figure 5.9 shows the comparison for the OH region near 1640 nm. In this wavelength range, both OH emission and CH_4 absorption lines are present, which makes the interpretation more complex. The model and the observed spectra both show the main OH features, but their relative strengths do not match perfectly. The simulated Earthshine spectra predict somewhat stronger OH emission than what is seen in the data, which could be related to temporal variability of the airglow. Since OH emission originates in the upper atmosphere, its intensity can change over short timescales (see Table 2.1). The overlap with nearby CH_4 lines may also affect the apparent shape of the features in the ratio spectra. Overall, the general structure of this region is reasonably reproduced by the model, though small mismatches are expected due to the variability

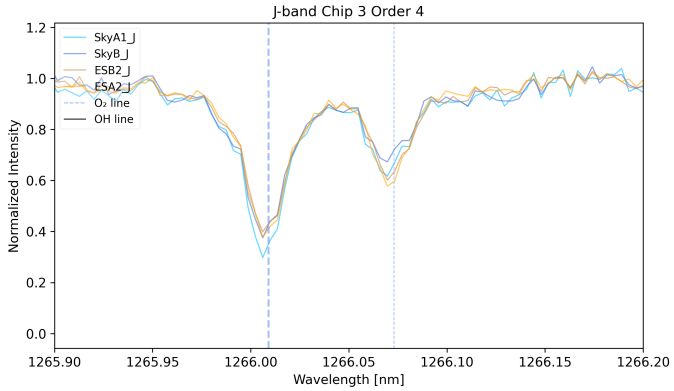

(a) Observed spectra (Earthshine and sky).

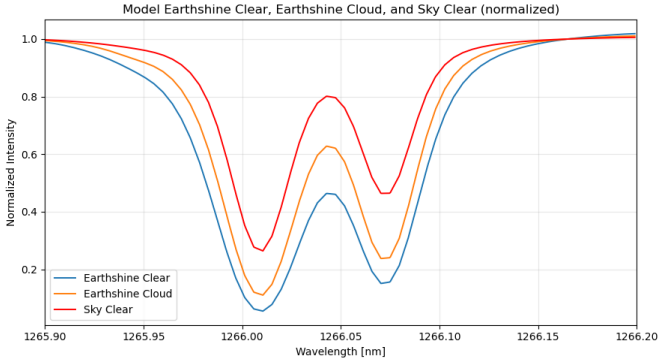

(b) Model spectra (Earthshine and sky, normalized).

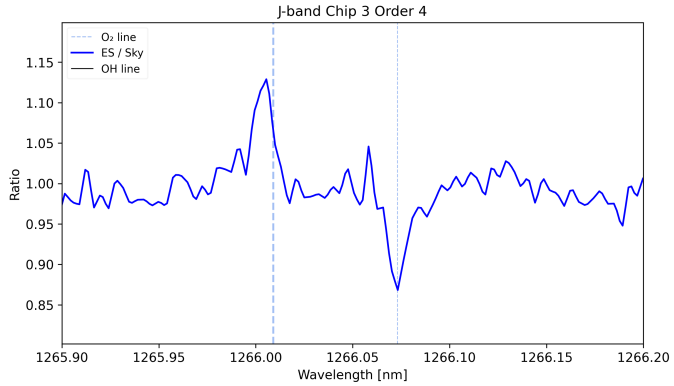

(c) Observed ES/Sky ratio.

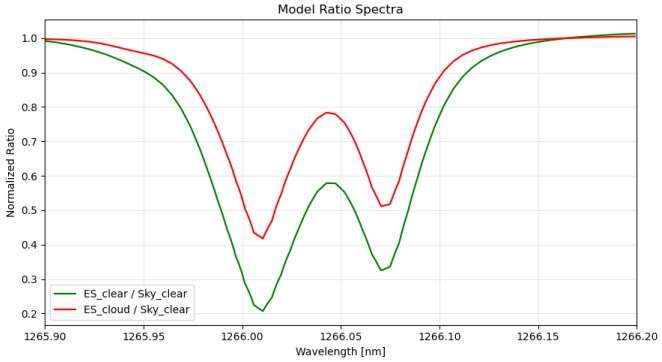

(d) Model ratios overlay: $\mathrm{ES}_{\mathrm{clear}}/\mathrm{Sky}_{\mathrm{clear}}$ and $\mathrm{ES}_{\mathrm{cloud}}/\mathrm{Sky}_{\mathrm{clear}}$.

Figure 5.7: Comparison between observed and modeled spectra in the O_2 region near 1266 nm. Panel (a) and (b) show the raw normalized spectra, while panel (c) and (d) present the ratio spectra.

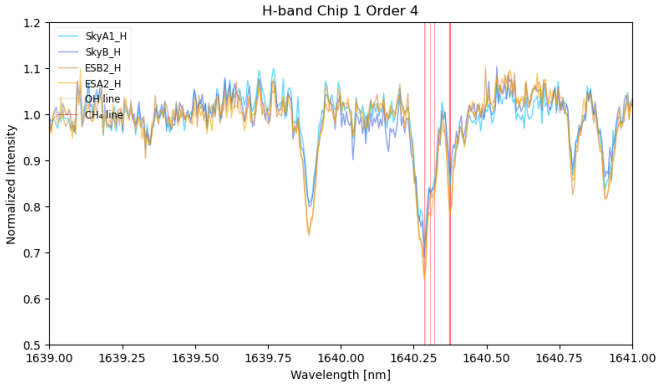

(a) Observed spectra (Earthshine and sky).

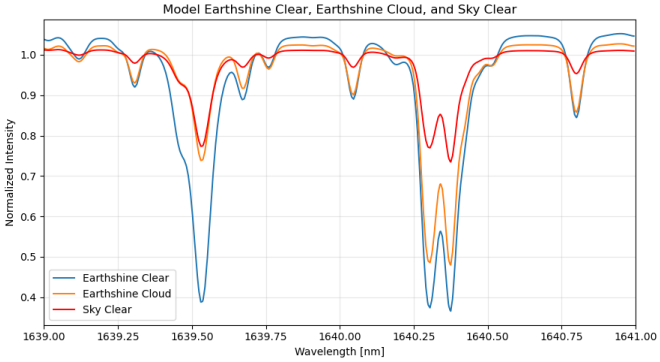

(b) Model spectra (Earthshine and sky, normalized).

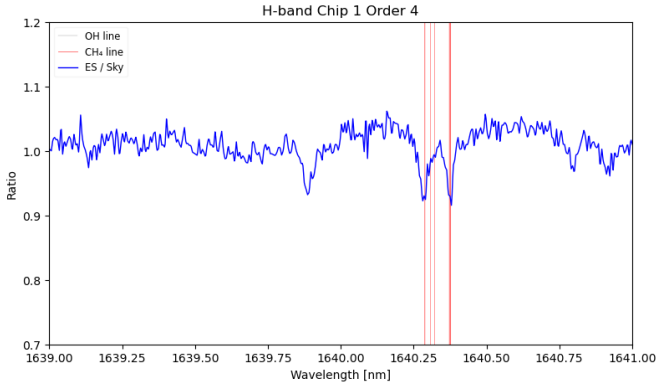

(c) Observed ES/Sky ratio.

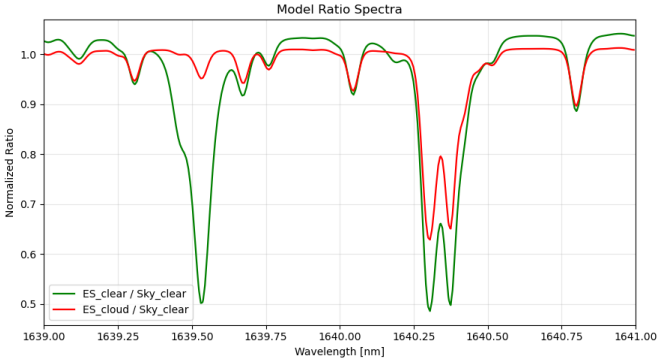

(d) Model ratios overlay: $\mathrm{ES_{clear}}/\mathrm{Sky_{clear}}$ and $\mathrm{ES_{cloud}}/\mathrm{Sky_{clear}}$.

Figure 5.8: Comparison between observed and modeled spectra in the CH_4 region near 1640 nm. Panel (a) and (b) show the raw normalized spectra, while panel (c) and (d) present the ratio spectra.

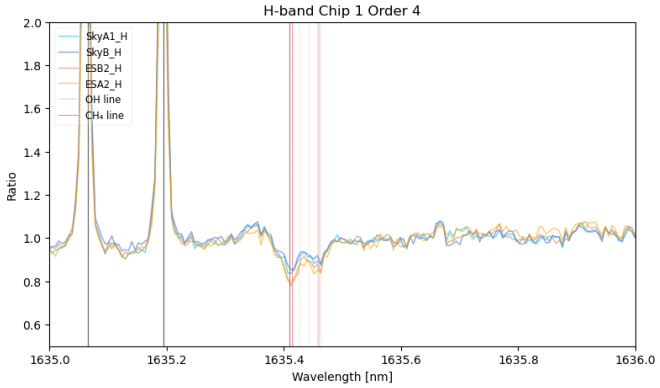

(a) Observed spectra (Earthshine and sky).

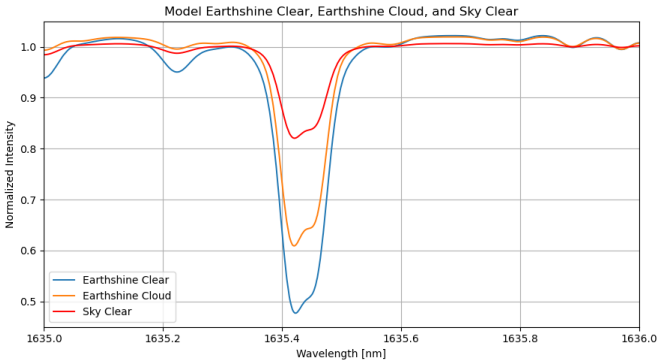

(b) Model spectra (Earthshine and sky, normalized).

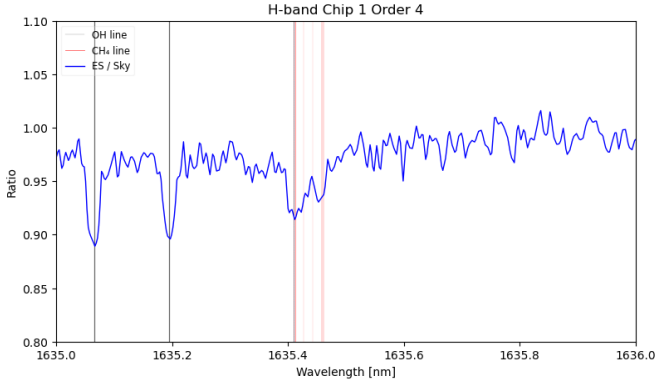

(c) Observed ES/Sky ratio.

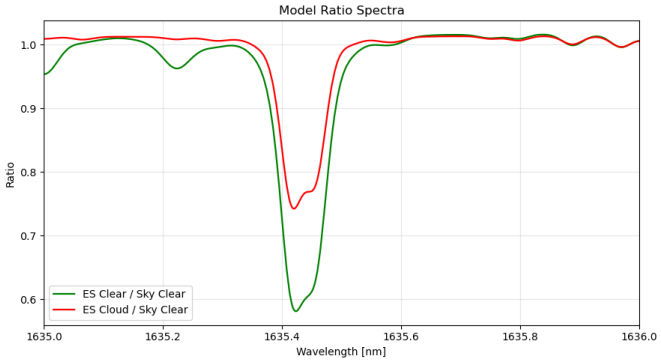

(d) Model ratios overlay: $\mathrm{ES}_{\mathrm{clear}}/\mathrm{Sky}_{\mathrm{clear}}$ and $\mathrm{ES}_{\mathrm{cloud}}/\mathrm{Sky}_{\mathrm{clear}}$.

Figure 5.9: Comparison between observed and modeled spectra in the OH region (H band, near 1640 nm). Panel (a) and (b) show the raw normalized spectra, while panel (c) and (d) present the ratio spectra.

Chapter 6

Discussion and Conclusion

This study aimed to investigate Earth as an exoplanet analog by using infrared Earthshine spectra observed with the CRIRES+ spectrograph at the VLT. With a resolution of $R \approx 100{,}000$, individual molecular absorption lines could be resolved and analyzed in detail. The main goal was to detect biosignature-related molecules such as O_2 and CH_4 and to understand how they appear in disk-integrated spectra of Earth.

The results indicate that the amplitude of the ES/Sky ratio spectra is systematically higher than in the ES/ES and Sky/Sky ratios for the J, H, and K bands. This behavior shows that the sky contribution was successfully minimized and that a residual Earthshine signal is still present in the ratios of ES/Sky. The strongest features were found for O_2 and CH_4, which together are considered one of the most important biosignature pairs. Additional biosignature-related molecules such as N_2O, as well as habitability-indicator gases like H_2O and CO_2, were also identified to give a more complete view of Earth's atmospheric composition. Comparison with radiative transfer simulations showed a general agreement across the tested molecular regions. In the J band near 1266 nm, the right-hand O_2 absorption line matched the model well, while the left-hand side deviated due to saturation. In the H band near 1640 nm, the cloudy model reproduced the CH_4 absorption depth more realistically, and the main OH emission features were also captured, though with different relative strengths likely caused by airglow variability.

In contrast to the other bands, the Y-band analysis did not show consistent results. Even after testing several different exposure pairs, the ES/Sky amplitudes did not appear higher than in the ES/ES and Sky/Sky ratios, as would be expected if the Earthshine signal were clearly present. This may be related to lower signal-to-noise, stronger contamination, or problems during the observing session.

A small Doppler shift caused by Earth's rotation was theocratically expected in the Earthshine spectra, but it was not detected. This could be due to the limited number of exposures or the mixing of signals from different parts of Earth's illuminated surface.

Overall, this work shows that high-resolution Earthshine spectroscopy can be used to detect biosignature-relevant molecules in integrated Earth spectra. The statistical comparison of amplitude distributions supported the interpretation that the Earthshine spectra contain additional features consistent with a real planetary signal, different from atmospheric effects.

This analysis also contributes to the preparation for future exoplanet characterization missions, which aim to detect and study terrestrial planets through their NIR spectra. Understanding how biosignatures appear in Earth's integrated spectra is a necessary step before applying similar methods to unresolved exoplanet observations. In this sense, the

present work provides an observational benchmark for future high-resolution studies of planetary atmospheres.

For future work, it would be better to analyze the data line by line instead of only using statistical distributions. In the current study, CH_4 and O_2 in the H band showed statistical importance; however, which exact lines contributed to this signal is not yet known. Identifying the individual lines responsible for these results would be the next step. This line-by-line approach would provide a clearer understanding of the ES/Sky spectra, and once established, the same methodology could be extended to exoplanetary observations. In addition, working with more detailed cloud simulations could improve the model–data comparison. Such detailed knowledge will be essential for future applications to exoplanets, where each detected line will provide valuable information about the planet's atmospheric composition and potential biosignatures. In this sense, this thesis serves as a first step and a guide showing where and how to look for biosignature features in high-resolution reflected-light spectra.

Appendix A

Full spectra and Simulations

A.1 Y-band full spectra

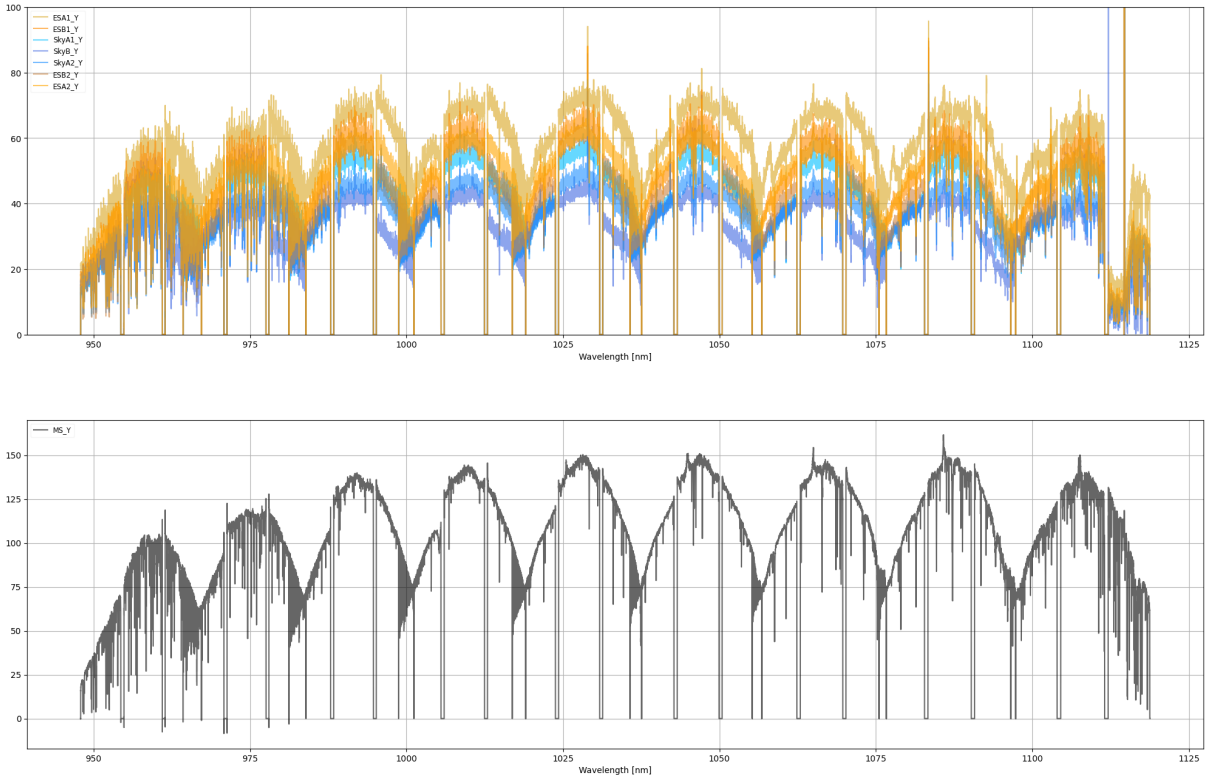

Figure A.1: Full Y-band spectra from 13 Nov 2021. Top: ESA/ESB & Sky frames. Bottom: MS frame.

A.2 J-band full spectra

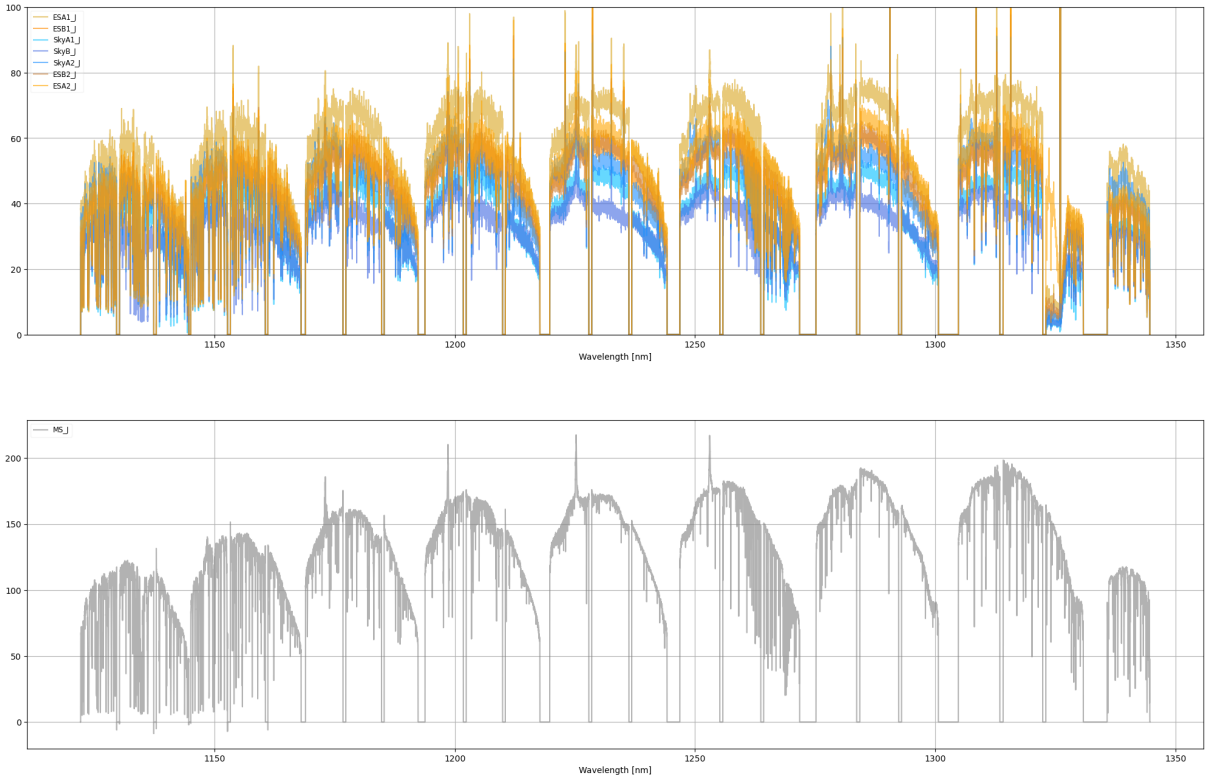

Figure A.2: Full J-band spectra from 13 Nov 2021. Top: ESA/ESB & Sky frames. Bottom: MS frame.

A.3 H-band full spectra

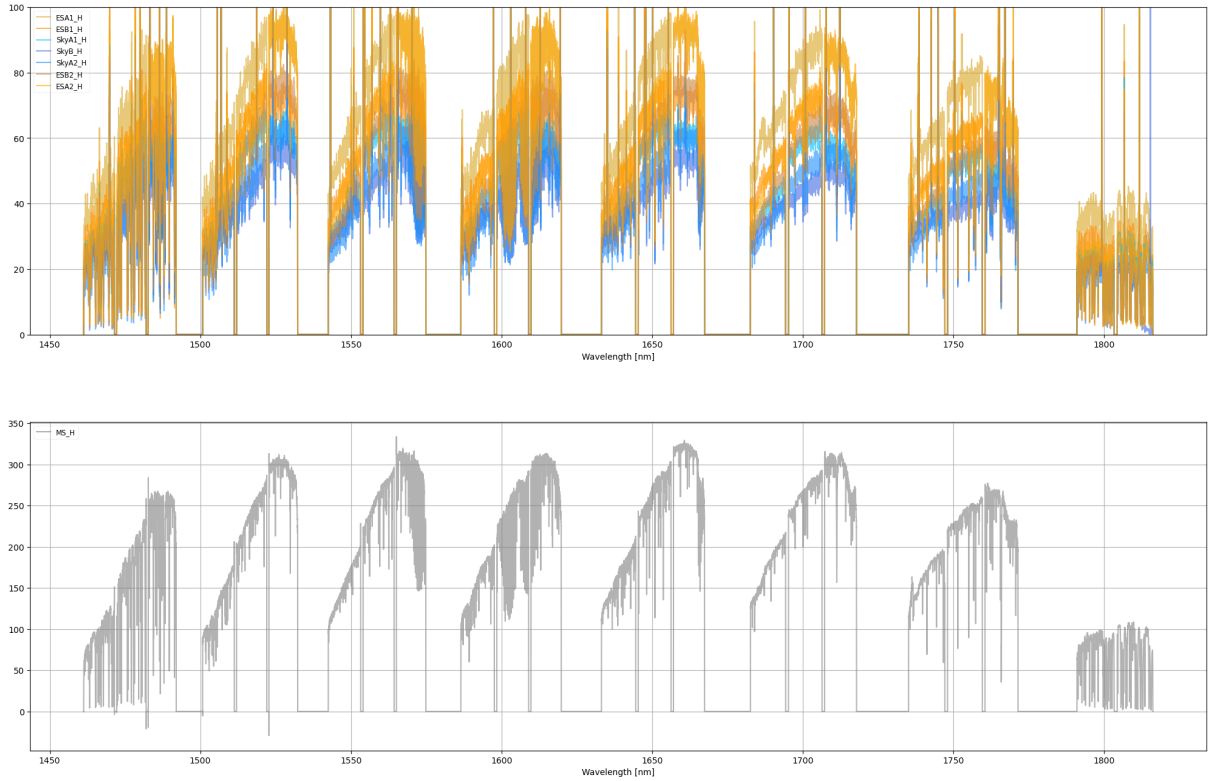

Figure A.3: Full H-band spectra from 13 Nov 2021. Top: ESA/ESB & Sky frames. Bottom: MS frame.

A.4 K-band full spectra

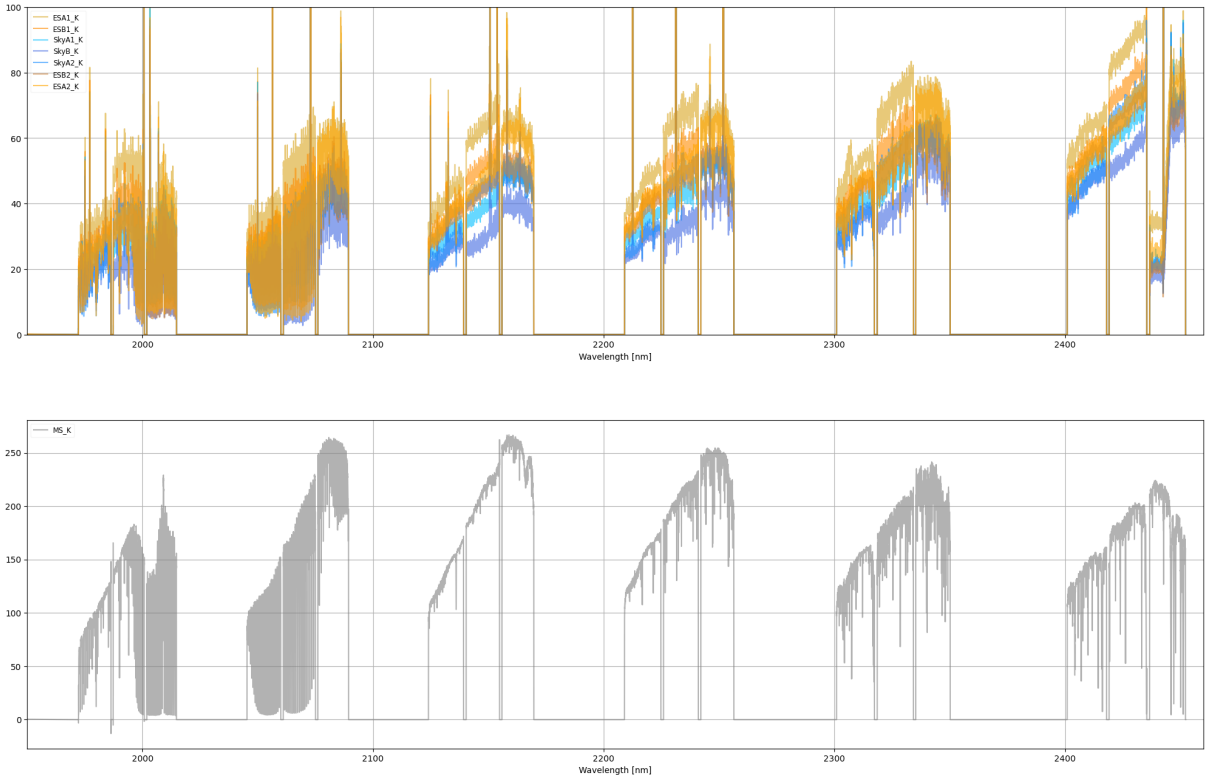

Figure A.4: Full K-band spectra from 13 Nov 2021. Top: ESA/ESB & Sky frames. Bottom: MS frame.

A.5 Radiative Transfer Simulations

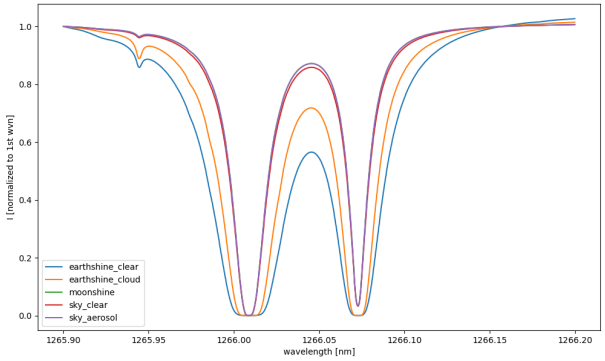

(a) O_2 region (1266 nm)

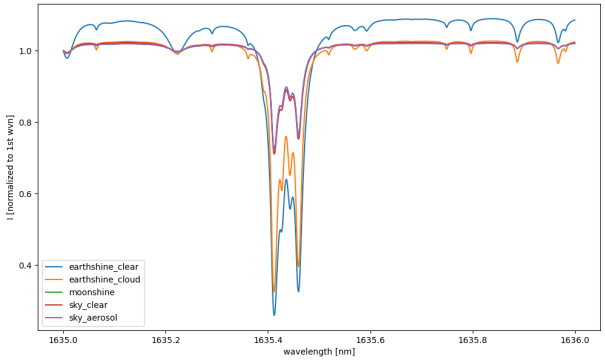

(b) OH region (1635 nm)

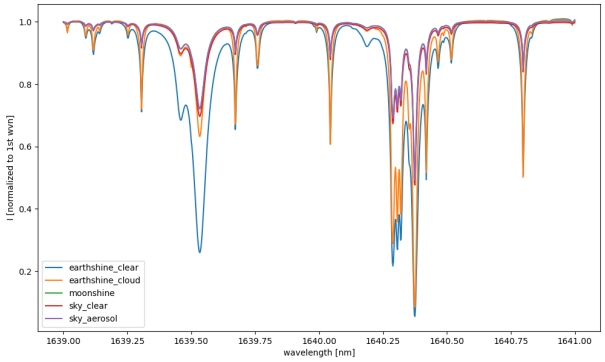

(c) CH_4 region (1640 nm)

Figure A.5: Original synthetic spectra produced by the radiative transfer simulations. Each plot shows five inputs: Earthshine clear, Earthshine cloud, Moonshine, Sky clear, and Sky aerosol.

Bibliography

[1] Hitran online. `https://hitran.org`. Accessed: 2025-09-25.

[2] G. P. Anderson, S. A. Clough, F. X. Kneizys, J. H. Chetwynd, and E. P. Shettle. Afgl atmospheric constituent profiles (0–120 km). Technical Report AFGL-TR-86-0110, Air Force Geophysics Laboratory, Hanscom Air Force Base, Bedford, MA, 1986.

[3] Theodore W. Anderson and Donald A. Darling. Asymptotic theory of certain "goodness of fit" criteria based on stochastic processes. *Annals of Mathematical Statistics*, 23(2):193–212, 1952.

[4] Luc Arnold, Serge Gillet, Olivier Lardière, Pierre Riaud, and Jean Schneider. A test for the search for life on extrasolar planets: Looking for the terrestrial vegetation signature in the earthshine spectrum. *Astronomy & Astrophysics*, 392:231–237, 2002.

[5] Robert E. Blankenship. *Molecular Mechanisms of Photosynthesis*. Wiley-Blackwell, Chichester, UK, 2nd edition, 2014.

[6] Craig F. Bohren and Donald R. Huffman. *Absorption and Scattering of Light by Small Particles*. Wiley, 1983.

[7] Donald E. Canfield. The early history of atmospheric oxygen: Homage to robert m. garrels. *Annual Review of Earth and Planetary Sciences*, 33, 2005.

[8] David C. Catling. The great oxidation event transition. In Heinrich D. Holland and Karl K. Turekian, editors, *Treatise on Geochemistry (Second Edition)*, volume 6, pages 177–193. Elsevier, Oxford, 2014.

[9] David C. Catling and James F. Kastiñg. *Evolution of the Earth' s Atmosphere*, page 169–326. Cambridge University Press, 2017.

[10] W. J. Conover. *Practical Nonparametric Statistics*. John Wiley & Sons, New York, 3rd edition, 1999.

[11] Leonardo da Vinci. *Codex Leicester: Notes on the Theory of the Earth and the Moon*. 1506. Facsimile edition, McGraw-Hill, New York, 1976.

[12] David W. Deamer and Gail R. Fleischaker. *Origins of Life: The Central Concepts*. Jones Bartlett Learning, 1994.

[13] David J. Des Marais, Martin O. Harwit, Kenneth W. Jucks, James F. Kasting, Douglas N. C. Lin, Jonathan I. Lunine, Jean Schneider, Sara Seager, Wesley A. Traub, and Neville J. Woolf. Remote sensing of planetary properties and biosignatures on extrasolar terrestrial planets. *Astrobiology*, 2(2):153–181, 2002.

[14] David J. Des Marais, Joseph A. Nuth, Louis J. Allamandola, Alan P. Boss, Jack D. Farmer, Tori M. Hoehler, Bruce M. Jakosky, Victoria S. Meadows, Andrew Pohorille, Bruce Runnegar, and Alfred M. Spormann. The nasa astrobiology roadmap. *Astrobiology*, 8(4), 2008.

[15] Claudia Emde, Robert Buras, and Bernhard Mayer. Alis: An efficient method to compute high spectral resolution polarized solar radiances using the monte carlo approach. *Journal of Quantitative Spectroscopy and Radiative Transfer*, 112(10):1622–1631, 2011.

[16] Claudia Emde, Robert Buras-Schnell, Arve Kylling, Bernhard Mayer, Josef Gasteiger, Ulrich Hamann, Jonas Kylling, Bettina Richter, Christian Pause, Timothy Dowling, and Luca Bugliaro. The libradtran software package for radiative transfer calculations (version 2.0.1). *Geoscientific Model Development*, 9:1647–1672, 2016.

[17] Claudia Emde, Robert Buras-Schnell, Michael Sterzik, and Stefano Bagnulo. Influence of aerosols, clouds, and sunglint on polarization spectra of earthshine. *Astronomy & Astrophysics*, 605:A2, 2017.

[18] European Southern Observatory. CRIRES+ user manual (document no. eso-323064). `https://www.eso.org/sci/facilities/paranal/instruments/crires/doc/ESO-323064_2_CRIRES+UserManual.pdf`, 2021. Accessed 2025-08-30.

[19] European Southern Observatory. Crires+ — a cross-dispersed upgrade to crires. `https://www.eso.org/sci/facilities/develop/instruments/crires_up.html`, 2021. Accessed: 2025-08-26.

[20] European Southern Observatory. Eso science archive. `https://archive.eso.org/cms.html`, 2025. Accessed: 2025-09-09.

[21] European Southern Observatory (ESO). Esoreflex. `https://www.eso.org/sci/software/esoreflex/`, 2025. Accessed 1 Oct 2025.

[22] Jean-Marie Flaud and Hermann Oelhaf. Infrared spectroscopy and the terrestrial atmosphere. *Comptes Rendus Physique*, 5(2):259–271, 2004.

[23] François Forget and Jeremy Leconte. Possible climates on terrestrial exoplanets. *Philosophical Transactions of the Royal Society A*, 371(1994):20130084, 2013.

[24] J.L. Grenfell, S. Gebauer, M. Godolt, K. Palczynski, H. Rauer, J. Stock, P. von Paris, R. Lehmann, and F. Selsis. Potential biosignatures in super-earth atmospheres ii. photochemical responses. *Astrobiology*, 13(5):415–438, May 2013.

[25] C. E. Harman, E. W. Schwieterman, J. C. Schottelkotte, and J. F. Kasting. Abiotic o2levels on planets around f, g, k, and m stars: Possible false positives for life? *The Astrophysical Journal*, 812(2):137, October 2015.

[26] C. Hermans, A. C. Vandaele, M. Carleer, S. Fally, R. Colin, B. Coquart, A. Jenouvrier, and M. F. Merienne. Absorption cross-sections of the collision-induced bands of oxygen from 34000 to 48000 cm^{-1} (0.21–0.29 µm). *Journal of Quantitative Spectroscopy and Radiative Transfer*, 62(3):283–296, 1999.

[27] Dian R. Hitchcock and James E. Lovelock. Life detection by atmospheric analysis. *Icarus*, 7(1):149–159, 1967.

[28] Lisa Kaltenegger, Wesley A. Traub, and Kenneth W. Jucks. Spectral evolution of an earth-like planet. *Astrophysical Journal*, 658:598–616, 2007.

[29] James F. Kasting. Earth's early atmosphere. *Science*, 259(5097):920–926, 1993.

[30] Charles D. Keeling, J. Fung Chin, and Timothy P. Whorf. Increased activity of northern vegetation inferred from atmospheric co_2 measurements. *Nature*, 382:146–149, 1996.

[31] Nancy Y. Kiang, Antígona Segura, Giovanna Tinetti, Govindjee, Robert E. Blankenship, Martin Cohen, Janet Siefert, David Crisp, and Victoria S. Meadows. Spectral signatures of photosynthesis. i. review of earth organisms. *Astrobiology*, 7(1):222–251, 2007.

[32] Daniel Kitzmann, Alexander B. C. Patzer, Philip von Paris, Mareike Godolt, Bastian Stracke, Sebastian Gebauer, John L. Grenfell, and Heike Rauer. Clouds in the atmospheres of extrasolar planets. i. climatic effects of multi-layered clouds for earth-like planets and implications for habitable zones. *Astronomy & Astrophysics*, 511:A66, 2010.

[33] Joshua Krissansen-Totton, David S. Bergsman, and David C. Catling. On detecting biospheres from chemical thermodynamic disequilibrium in planetary atmospheres. *Astrobiology*, 16(1):39–67, January 2016.

[34] K. N. Liou. *An Introduction to Atmospheric Radiation*, volume 26 of *International Geophysics Series*. Academic Press, New York, 1980.

[35] Kuo-Nan Liou. *An Introduction to Atmospheric Radiation*. Academic Press, 2nd edition, 2002.

[36] Timothy A. Livengood, L. Drake Deming, Michael F. A'Hearn, David Charbonneau, Tilak Hewagama, Carey M. Lisse, Lucy A. McFadden, Victoria S. Meadows, Tyler D. Robinson, Sara Seager, and Dennis D. Wellnitz. Properties of an earth-like planet orbiting a sun-like star: Earth observed by the epoxi mission. *Astrobiology*, 11(9), 2011.

[37] J. E. Lovelock and I. R. Kaplan. Thermodynamics and the recognition of alien biospheres [and discussion]. *Proceedings of the Royal Society of London. Series B, Biological Sciences*, 189(1095):167–181, 1975.

[38] James E. Lovelock. A physical basis for life detection. *Nature*, 207:568–570, 1965.

[39] Timothy W. Lyons, Christopher T. Reinhard, and Noah J. Planavsky. The rise of oxygen in earth's early ocean and atmosphere. *Nature*, 506(7488), 2014.

[40] Belén Maté, C. L. Lugez, A. M. Solodov, G. T. Fraser, and W. J. Lafferty. Investigation of the collision-induced absorption by o_2 near 6.4 μm in pure o_2 and o_2–n_2 mixtures. *Journal of Geophysical Research: Atmospheres*, 105(D17):22225–22230, 2000.

[41] B. Mayer. Radiative transfer in the cloudy atmosphere. *European Physical Journal Conferences*, 1:75–99, 2009.

[42] B. Mayer and A. Kylling. Technical note: The libradtran software package for radiative transfer calculations—description and examples of use. *Atmospheric Chemistry and Physics*, 5:1855–1877, 2005.

[43] Victoria S. Meadows. Modelling the diversity of extrasolar terrestrial planets. *Proceedings IAU Colloquium No. 200: Direct Imaging of Exoplanets: Science & Techniques*, pages 25–34, 2006.

[44] Victoria S. Meadows. Reflections on o_2 as a biosignature in exoplanetary atmospheres. *Astrobiology*, 17(10):1022–1052, 2017.

[45] Victoria S. Meadows, Christopher T. Reinhard, Giada N. Arney, Mary N. Parenteau, Edward W. Schwieterman, Shawn D. Domagal-Goldman, Andrew P. Lincowski, Karl R. Stapelfeldt, Heike Rauer, Shiladitya DasSarma, Supriya Hegde, Norio Narita, Russell Deitrick, Jacob Lustig-Yaeger, and Timothy W. Lyons. Exoplanet biosignatures: Understanding oxygen as a biosignature in the context of its environment. *Astrobiology*, 18(6):630–662, 2018.

[46] Pilar Montañés-Rodríguez, Enric Pallé, Philip R. Goode, and F. Javier Martín-Torres. Vegetation signature in the observed globally integrated spectrum of earth considering simultaneous cloud data: Applications for extrasolar planets. *The Astrophysical Journal*, 651(1):544–552, 2006.

[47] Douglas C. Montgomery and George C. Runger. *Applied Statistics and Probability for Engineers*. John Wiley & Sons, Hoboken, NJ, 7th edition, 2018. Seventh Edition.

[48] Gunnar Myhre, Drew Shindell, F.-M. Bréon, William Collins, Jan Fuglestvedt, Jianping Huang, Dorothy Koch, Jean-Francois Lamarque, Dorothy Lee, Bruno Mendoza, Teruyuki Nakajima, Alan Robock, Graeme Stephens, Toshihiko Takemura, and Hua Zhang. Anthropogenic and natural radiative forcing. In T. F. Stocker, D. Qin, G.-K. Plattner, M. Tignor, S. K. Allen, J. Boschung, A. Nauels, Y. Xia, V. Bex, and P. M. Midgley, editors, *Climate Change 2013: The Physical Science Basis. Contribution of Working Group I to the Fifth Assessment Report of the Intergovernmental Panel on Climate Change*, pages 659–740. Cambridge University Press, Cambridge, UK, 2013.

[49] NASA Astrobiology. About — life detection. `https://astrobiology.nasa.gov/research/life-detection/about/`, n.d. Defines life as "a self-sustaining chemical system capable of Darwinian evolution.".

[50] NASA Ozone Watch. Ozone facts: Stratospheric "good" ozone. `https://ozonewatch.gsfc.nasa.gov/facts/SH.html`, 2024. Last updated 2024-09-23; accessed 2025-09-06.

[51] NASA/IPAC Extragalactic Database (NED). Statistics and the treatment of experimental data: 2.3 the gaussian or normal distribution. Caltech/IPAC Level 5. Accessed 1 Oct 2025.

[52] E. Pallé, M. R. Zapatero Osorio, R. Barrena, P. Montañés-Rodríguez, and E. L. Martín. Earth's transmission spectrum from lunar eclipse observations. *Nature*, 459:814–816, 2009.

[53] Heike Rauer, Silke Gebauer, Paul V. Paris, Juan Cabrera, Mareike Godolt, John L. Grenfell, Adrian Belu, Franck Selsis, Pascal Hedelt, and Franz Schreier. Potential biosignatures in super-earth atmospheres. i. spectral appearance of super-earths around m dwarfs. *Astronomy & Astrophysics*, 529:A8, 2011.

[54] C. Richard, I. E. Gordon, L. S. Rothman, M. Abel, L. Frommhold, M. Gustafsson, J.-M. Hartmann, C. Hermans, W. J. Lafferty, G. S. Orton, K. M. Smith, and H. Tran. New section of the hitran database: Collision-induced absorption (cia) and complex refractive index of aerosols. *Journal of Quantitative Spectroscopy and Radiative Transfer*, 113:1276–1285, 2012.

[55] Tyler D. Robinson, Victoria S. Meadows, and David Crisp. Detecting oceans on extrasolar planets using the glint effect. *The Astrophysical Journal Letters*, 721(1):L67–L71, 2010.

[56] Giulia Roccetti, Claudia Emde, Michael F. Sterzik, Mihail Manev, Julia V. Seidel, and Stefano Bagnulo. Planet earth in reflected and polarized light i. 3d radiative transfer simulations of realistic surface-atmosphere systems, April 2025.

[57] Giulia Roccetti, Michael F. Sterzik, Julia V. Seidel, Claudia Emde, Mihail Manev, and Stefano Bagnulo. Planet earth in reflected and polarized light. ii. refining contrast estimates for rocky exoplanets with elt and hwo. *Astronomy & Astrophysics*, 700:A62, 2025.

[58] F. Rodler, A. Brucalassi, and E. Valenti. *CRIRES User Manual*. European Southern Observatory, Garching, Germany, 2025. ESO Document No. ESO-254264, Version P116.1, Published 22 May 2025.

[59] Sarah Rugheimer, Lisa Kaltenegger, Antígona Segura, Jeffrey Linsky, and Subhanjoy Mohanty. Uv surface environments and atmospheres of earth-like planets orbiting m dwarfs. *The Astrophysical Journal*, 809(1):57, 2015.

[60] Sarah Rugheimer, Lisa Kaltenegger, Antígona Segura, Jeffrey Linsky, and Subhanjoy Mohanty. Uv surface environment of earth-like planets orbiting fgkm stars through geological evolution. *Astrophysical Journal*, 809(1):57, 2015.

[61] Carl Sagan, W. Reid Thompson, Robert Carlson, Donald Gurnett, and Charles Hord. A search for life on earth from the galileo spacecraft. *Nature*, 365(6448):715–721, 1993.

[62] E. W. Schwieterman, V. S. Meadows, S. D. Domagal-Goldman, D. Deming, G. N. Arney, R. Luger, C. E. Harman, A. Misra, and R. Barnes. Identifying planetary biosignature impostors: Spectral features of co and o_4 resulting from abiotic o_2 and o_3 production. *The Astrophysical Journal Letters*, 819(1):L13, 2016.

[63] Edward W. Schwieterman. *Surface and Temporal Biosignatures*, page 3173–3201. Springer International Publishing, 2018.

[64] Edward W. Schwieterman, Nancy Y. Kiang, Mary N. Parenteau, Chester E. Harman, Shiladitya DasSarma, Theresa M. Fisher, Giada N. Arney, Hilairy E. Hartnett, Christopher T. Reinhard, Stephanie L. Olson, Victoria S. Meadows, Charles S. Cockell, Sara I. Walker, John Lee Grenfell, Siddharth Hegde, Sarah Rugheimer, Renyu Hu,

and Timothy W. Lyons. Exoplanet biosignatures: A review of remotely detectable signs of life. *Astrobiology*, 18(6):663–708, 2018.

[65] S. Seager, W. Bains, and R. Hu. Biosignature gases in h2-dominated atmospheres on rocky exoplanets. *The Astrophysical Journal*, 777(2):95, October 2013.

[66] Sara Seager. *Exoplanet Atmospheres: Physical Processes*. Princeton University Press, 2010.

[67] Sara Seager, Matthew Schrenk, and William Bains. An astrophysical view of earth-based metabolic biosignature gases. *Astrobiology*, 12(1):61–82, 2012.

[68] Sara Seager, Edwin L. Turner, James Schafer, and Eric B. Ford. Vegetation's red edge: A possible spectroscopic biosignature of extraterrestrial plants. *Astrobiology*, 5(3):372–390, 2005.

[69] Antígona Segura, James F. Kasting, Victoria S. Meadows, Martin Cohen, John Scalo, David Crisp, Richard A. H. Butler, and Giovanna Tinetti. Biosignatures from earth-like planets around m dwarfs. *Astrobiology*, 5(6), 2005.

[70] Michael F. Sterzik, Stefano Bagnulo, and Enric Palle. Biosignatures as revealed by spectropolarimetry of earthshine. *Nature*, 483(7387):64–66, 2012.

[71] Michael F. Sterzik, Stefano Bagnulo, Daphne M. Stam, Claudia Emde, and Mihail Manev. Spectral and temporal variability of earth observed in polarization. *Astronomy & Astrophysics*, 622:A41, 2019.

[72] Roger Summons, Pierre Albrecht, Gene McDonald, and J̃ohn Moldowan. Molecular biosignatures. *Space Science Reviews*, 135:133–159, 03 2008.

[73] Jill Tarter. The search for extraterrestrial intelligence (seti). *Annual Review of Astronomy and Astrophysics*, 45, 2007.

[74] Rudolf K. Thauer, Michael Kühl, Uwe Deppenmeier, and Norbert Pfennig. Methanogenic archaea: ecologically relevant differences in energy conservation. *Nature Reviews Microbiology*, 6(8):579–591, 2008.

[75] Maggie A. Thompson, Joshua Krissansen-Totton, Nicholas Wogan, Myriam Telus, and Jonathan J. Fortney. The case and context for atmospheric methane as an exoplanet biosignature. *Proceedings of the National Academy of Sciences*, 119(14), March 2022.

[76] Margaret C. Turnbull, Wesley A. Traub, Kenneth W. Jucks, Neville J. Woolf, Michael R. Meyer, Nadya Gorlova, Michael F. Skrutskie, and John C. Wilson. Spectrum of a habitable world: Earthshine in the near-infrared. *The Astrophysical Journal*, 644(1):551–559, 2006.

[77] Katharina Uhlmannsiek. Tracing airglow as biosignature of planet earth with high-resolution infrared spectroscopy. Master's thesis, Ludwig-Maximilians-Universität München, Fakultät für Physik, München, June 2023.

[78] Geoffrey K. Vallis. *Atmospheric Planetary Science: Fundamentals and Applications*. Springer, Cham, 2021.

[79] Christian von Savigny. Airglow in the earth atmosphere: basic characteristics and excitation mechanisms. *ChemTexts*, 3(4):1–14, Oct 2017.

[80] John Walker. Earth and moon viewer. `https://www.fourmilab.ch/earthview/`, 2025. Accessed: 2025-09-30.

[81] J. M. Wallace and P. V. Hobbs. *Atmospheric Science: An Introductory Survey*. Academic Press, San Diego, 2nd edition, 2006.

[82] Eric W. Weisstein. Gaussian function. From MathWorld—A Wolfram Resource, 2025. Accessed 1 Oct 2025.

[83] Sabine Wüst, Michael Bittner, Patrick J. Espy, W. John R. French, and Frank J. Mulligan. Hydroxyl airglow observations for investigating atmospheric dynamics: results and challenges. *Atmospheric Chemistry and Physics*, 23(2):1599–1618, 2023.

Declaration of Originality

I declare that the work presented in this thesis is my own and has been carried out independently, except where explicit reference is made to the work of others. In writing this thesis, I used generative artificial intelligence tools, specifically *ChatGPT-5* (for Python plotting assistance and debugging) and the *Overleaf AI assistant* (for grammar and language corrections). These tools were used solely to support technical and linguistic refinement. All scientific analyses, interpretations, and conclusions are entirely my own.

Bologna, October 16, 2025

Yaren Hediye Bektaş